Water Resources Research

RESEARCH ARTICLE
10.1029/2021WR031044

Key Points:

- Theoretical 3D spectral solutions of the groundwater flow equation are enhanced by adding dominant frequencies in the pre-assigned spectrum
- Dominant frequencies on the top boundary pressure head are identified with a robust statistical technique including significance levels
- Groundwater fluxes and residence time distributions are better captured with the inclusion of dominant frequencies in the spectral solutions

Supporting Information:

Supporting Information may be found in the online version of this article.

Correspondence to:

G. Perez,
gabriel.perez.mesa@vanderbilt.edu

Citation:

Perez, G., Gomez-Velez, J. D., Chen, X., Scheibe, T., Chen, Y., & Bao, J. (2021). Identification of characteristic spatial scales to improve the performance of analytical spectral solutions to the groundwater flow equation. *Water Resources Research*, *57*, e2021WR031044. https://doi.org/10.1029/2021WR031044

Received 15 AUG 2021
Accepted 3 DEC 2021

Author Contributions:

Conceptualization: Gabriel Perez, Jesus D. Gomez-Velez
Data curation: Gabriel Perez, Jesus D. Gomez-Velez, Yunxiang Chen, Jie Bao
Formal analysis: Gabriel Perez
Funding acquisition: Jesus D. Gomez-Velez, Xingyuan Chen, T. Scheibe
Investigation: Gabriel Perez, Jesus D. Gomez-Velez, Xingyuan Chen, T. Scheibe, Yunxiang Chen, Jie Bao
Methodology: Gabriel Perez, Jesus D. Gomez-Velez
Project Administration: Jesus D. Gomez-Velez, Xingyuan Chen, T. Scheibe, Yunxiang Chen, Jie Bao
Resources: Jesus D. Gomez-Velez, Xingyuan Chen, T. Scheibe

Identification of Characteristic Spatial Scales to Improve the Performance of Analytical Spectral Solutions to the Groundwater Flow Equation

Gabriel Perez[1], Jesus D. Gomez-Velez[1,2,3], Xingyuan Chen[4], T. Scheibe[4], Yunxiang Chen[4], and Jie Bao[4]

[1]Department of Civil and Environmental Engineering, Vanderbilt University, Nashville, TN, USA, [2]Department of Earth and Environmental Sciences, Vanderbilt University, Nashville, TN, USA, [3]Consortium for Risk Estimation With Stakeholder Participation, Vanderbilt University, Nashville, TN, USA, [4]Pacific Northwest National Laboratory, Richland, WA, USA

Abstract Analytical solutions for the three-dimensional groundwater flow equation have been widely used to gain insight about subsurface flow structure and as an alternative to computationally expensive numerical models. Of particular interest are solutions that decompose prescribed hydraulic head boundaries (e.g., Dirichlet boundary condition) into a collection of harmonic functions. Previous studies estimate the frequencies and amplitudes of these harmonics with a least-square approach where the amplitudes are fitted given a pre-assigned set of frequencies. In these studies, an ad hoc and structured discretization of the frequency domain is typically used, excluding dominant frequencies while assigning importance to spurious frequencies, with significant consequences for estimating the fluxes and residence times. This study demonstrates the advantages of using a pre-assigned frequency spectrum that targets the dominant frequencies based on rigorous statistical analysis with predefined significance levels. The new approach is tested for three hydrologic conceptualizations: (a) a synthetic periodic basin, (b) synthetic bedforms, and (c) a natural mountainous watershed. The performance of the frequency spectrum selection is compared with exact analytical or approximate numerical solutions. We found that the new approach better describes the fluxes and residence times for Dirichlet boundaries with well-defined characteristics spatial scales (e.g., periodic basins and bedforms). For more complex scenarios, such as natural mountainous watersheds, both pre-assigned frequency spectrums present similar performance. The spectral solutions presented here can play a central role in developing reduced-complexity models for assessing regional water and solute fluxes within mountain watersheds and hyporheic zones.

1. Introduction

Groundwater and surface water continuously exchange water, solutes, and energy over a wide range of spatial and temporal scales (Cardenas, 2008; Gomez & Wilson, 2013; Gomez-Velez & Harvey, 2014; Tóth, 2009; Winter et al., 1998; Wörman et al., 2007). This connection results in a nested and multiscale flow field that exerts a first-order control on water quantity and quality (Cardenas, 2008; Knapp et al., 2003), weathering and landscape evolution (Frisbee et al., 2013; Maher & Chamberlain, 2014; White & Brantley, 2003), and ecosystem functioning (Harvey, 2016; Harvey et al., 2019). For example, at the basin scale, groundwater flow is primarily driven by spatiotemporal variations of the water table, which, at the same time, are the result of the complex configuration of net recharge and the constraining effect of surface water bodies (e.g., rivers and lakes) (Tóth, 2009; Wörman et al., 2006, 2007). This basin-scale flow system is part of continuum that connects to and constrains the exchange occurring along the river corridors, where water flow paths originate from and end at the main channel (Gomez-Velez et al., 2017; Harvey et al., 2019; Harvey & Gooseff, 2015; Mojarrad et al., 2019). An example of this local-scale exchange process is bedform-driven hyporheic exchange, which is driven by hydraulic head variations induced by the interaction of water column flow with a complex streambed topography (Boano et al., 2014).

A common conceptualization to describe the connection between groundwater and surface water and the resulting multiscale groundwater flow system is prescribing the hydraulic head as a top boundary (Tóth, 2009; Wörman et al., 2006, 2007). In the case of regional groundwater flow and bedform-driven hyporheic exchange, the topography can be used as a proxy for this hydraulic head. For example, at the basin scale, the water table is used to characterize the hydraulic head, which is partially controlled by the surface topography. In fact, in humid regions, where the recharge rate is sufficiently higher than the infiltration capacity of the ground, the water table can be

Software: Gabriel Perez
Supervision: Jesus D. Gomez-Velez
Validation: Gabriel Perez
Visualization: Gabriel Perez
Writing – original draft: Gabriel Perez
Writing – review & editing: Gabriel Perez, Jesus D. Gomez-Velez, Xingyuan Chen, T. Scheibe, Yunxiang Chen, Jie Bao

classified as "topography-controlled," which allow us to reasonably assume that it is a subdued and smoothed version of the topography (Caruso et al., 2016; Condon & Maxwell, 2015; Gleeson et al., 2011; Haitjema & Mitchell-Bruker, 2005; Toth, 1963). In other words, the hydraulic head is fully defined by the landscape's topography. At the scale of bedforms, the interplay between channel flow and the streambed topography produces pressure variations along the sediment-water interface (SWI) that drive hyporheic exchange. These pressure variations are strongly correlated to bathymetry (Elliott & Brooks, 1997a, 1997b; Fehlman, 1985; H. W. Shen et al., 1990). To put it in another way, the streambed topography can be used to approximate the spatial distribution of hydraulic head at the SWI.

Given the analytical tractability of the steady-state groundwater flow equation (i.e., a Laplace equation) for cases where a Dirichlet boundary condition is used, several authors have proposed analytical solutions to cases where the top boundary condition for the modeling domain (i.e., a box domain bounded by the water table or the SWI at the top boundary) is a prescribed hydraulic head that depends on the topography (Elliott & Brooks, 1997b; Toth, 1962; Packman & Bencala, 2000; Zijl, 1999). A particularly important example is the analytical solution presented by Wörman et al. (2006) for steady-state, three-dimensional groundwater flow within an infinite, homogeneous, and isotropic domain. Wörman et al. (2006) solution provides the hydraulic head field as a function of a spectral decomposition of an arbitrary hydraulic head distribution at the top boundary. Marklund and Wörman (2011) extended this spectral solution to systems with anisotropic, depth-decaying and layered permeability. For simplicity, we refer to these three-dimensional solutions based on spectral decomposition as *spectral solutions*.

The use of spectral solutions is appealing in groundwater modeling because it provides a reliable and computationally efficient alternative to numerical models for groundwater systems while providing a detailed accounting of the role of the different scales of the hydraulic head at the top of the domain and their contribution to flow. In other words, it allows us to link the characteristic topographic scales with the multiscale flow systems from large (e.g., regional flows cells) to small (e.g., hyporheic flow cells) scales (Wang, 2021, under review). For instance, Stonedahl et al. (2010) explored with three different orthogonal basis of sines and cosines to model subsurface flow induced by bedforms up to larger geomorphologic features such as meanders. They indicate that the net interfacial flux and spatial distribution of hyporheic exchange are controlled by the complex topographic interactions between small and larger scales, demonstrating that the spatial patterns and rates of hyporheic exchange cannot be well represented by simplified versions of the stream topography. Regarding larger spatial scales, Caruso et al. (2016) used a spectral solution to demonstrate that the structure of the water table causes a strong spatial variability of the upwelling groundwater along the river corridor, using the Borbore basin in Italy as a proof of concept. This result exposed the influence of the landscape topographic structure on the regional discharge fluxes to the river network and its effect on hyporheic exchange fluxes. Along the same lines, Mojarrad et al. (2019) quantified the effects of regional groundwater fluxes discharging to channels and how they influence hyporheic exchange fluxes over 14 reaches in first-, second-, third-, and fifth-order streams. Their groundwater flow model includes not only the previous spectral solutions but also accounts for the hydrostatic and dynamic head fluctuations induced by the streambed topography (Elliott & Brooks, 1997a).

The performance of these spectral solutions depends on how well the spectral decomposition represents all the spatial scales characterizing the hydraulic head at the top boundary. In general, the spectral solution is based on three key components: (a) definition of the orthogonal basis, (b) definition of a pre-assigned frequency spectrum, and (c) estimation of the Fourier coefficients. These components are further illustrated in Section 2. The implementation of the spectral solution, however, is not trivial because the approach used for each of the components above can introduce artifacts in the analysis, which introduce artificial or remove/smear real fluctuation in the representation of the top hydraulic head boundary. These artifacts can alter the total amount of exchange and the relative contribution of local, intermediate, and regional flow paths as well as residence times.

The trade-off between the strategy used for the spectral reconstruction of the top boundary's hydraulic head presents challenges similar to the ones encountered in the definition of a numerical discretization mesh for hydrologic modeling (C. Wang et al., 2018). A finer mesh will better capture changes in topographic gradients and domain boundaries at the expense of increasing the computational cost, which from a computational burden perspective is analogous to increasing the number of Fourier coefficients used to define the pre-assigned frequency spectrum for spectral method. However, the spectral decomposition poses an additional challenge because indiscriminately exploring a wider range of frequencies without focusing on the critical wavelengths characterizing the target function can result in spectral leakage (Crockett, 2019), where critical scales lose spectral power while spurious ones become important. The proper representation of the top boundary hydraulic head or domain boundaries is critical in groundwater modeling given its role defining key features such as rivers, ridges, and bedforms among others. Poor representation of these features leads to inadequate representations of hyporheic fluxes (Chow et al., 2019), groundwater recharge (Stoertz & Bradbury, 1989), water table depths and soil water storage (Sulis et al., 2011), soil moisture content in wet periods (Kuo et al., 1999), inundation extent and contaminant biochemical and ecological processes (C. Shen et al., 2016), and river base flow and its residence time and solute concentrations (C. Wang et al., 2018).

Our research hypothesis is that *current spectral solutions used for the analysis of surface-groundwater flow systems can be significantly improved by including dominant frequencies in the representation of the hydraulic head at the top boundary, providing better estimates of groundwater fluxes and residence times*. To test this hypothesis, we present a robust methodology to define the pre-assigned spectrum based on the identification of dominant and statistically significant frequencies of the two-dimensional Fourier power spectrum. Our specific objectives are to (a) integrate dominant frequencies identified by spectral analysis techniques into spectral solutions of the surface-groundwater flow system, (b) quantify the benefit in including dominant frequencies into spectral solutions in terms of groundwater fluxes and residence times, and (c) test and validate the inclusion of dominant frequencies in spectral solutions under different topographic scenarios.

As a proof of concept, we compare the ability of the traditional and new approach to reproduce flow fields and residence time distributions (RTDs) in three different systems: (a) a synthetic periodic basin, (b) synthetic sandy bedforms, and (c) a natural mountainous watershed. Our results are compared with exact analytical or numerical solutions.

The rest of the study is organized as follows. Section 2 describes the spectral solutions, including the new procedure to identify dominant frequencies from the topography. Section 3 describes the three systems used as case studies and their topographies as well as the analytical and numerical solutions used to validate our results. This is followed by a detailed description of the results in Section 3, where we focus on the differences in the flow field, the spatial distribution of recharge/discharge areas, and the RTDs. The implications of this study are addressed in a discussion section (Section 5), and finally, we highlight the main contributions of this study in Section 6.

2. Materials and Methods

2.1. Spectral Solution for the Groundwater Flow Equation

Steady-state groundwater flow for a homogeneous and isotropic porous media is described by the Laplace Equation $\nabla^2 \mathrm{h} = 0$, where $h(x, y, z)$ is the hydraulic head [L] at location $\mathbf{x} = [x, y, z]$ [L] (Bear, 1975). This linear operator is amenable to analytical treatment using superposition for a myriad of boundary conditions. For example, a widely used conceptualization assumes an infinite domain in the horizontal plane ($x - y$ plane) bounded in the vertical at $z = 0$, where the head distribution is prescribed, and $z = -\varepsilon$, where ε is a depth where the aquifer becomes impervious [L]. Mathematically, these constraints are represented by the following boundary conditions: $h(x, y, z = 0) = H(x, y)$ and $\partial h / \partial z|_{z=-\varepsilon} = 0$. In this case, the hydraulic head distribution at the top of the domain $H(x, y)$ represents the position of the water table for watershed-scale modeling or the hydraulic head at the sediment-water interface (SWI) for the modeling of bedform-driven hyporheic exchange. Under these boundary conditions, and using the principle of superposition, the Laplace equation can be solved analytically when $H(x, y)$ is described as a linear combination of harmonic functions (Kreyszig, 2014).

A common approach uses the Fourier series to represent $H(x, y)$ as a sum of harmonics each with different amplitude and frequency. The solution in this case is known as the *spectral solution*, and it allows us to obtain an interpretable analytical solution where the contributions of each characteristic scale of the top boundary condition can be traced to any point within the domain for the hydraulic head and flow (Toth, 1962; Wörman et al., 2006; Zijl, 1999).

For example, Wörman et al. (2006) derived an analytical solution for the hydraulic head when the top boundary condition $H(x, y)$ is decomposed into orthogonal basis of the form $\sin(k_{xi} x) \cos(k_{yj} y)$:

$$h(x, y, z) = \langle h \rangle + \sum_{j=1}^{N_y} \sum_{i=1}^{N_x} (h_m)_{i,j} \frac{(\exp[zA] + \exp[(-2\varepsilon - z)A])}{1 + \exp(-2\varepsilon A)} \sin(k_{xi} x)\, cos\,(k_{yj} y) \qquad (1)$$

where $\langle h \rangle$ is the mean value of $H(x, y)$ [L], N_x and N_y are the number of harmonic functions used in the orthogonal basis (usually $N_x = N_y$), $(h_m)_{i,j}$ is the amplitude coefficient (or Fourier coefficient) [L] for the spatial frequencies (or wavenumbers) k_{xi} and k_{y_i} in the x and y directions [L^{-1}], respectively, and $A = \sqrt{k_{x_i}^2 + k_{y_j}^2}$ is the radial spatial frequency [L^{-1}]. We can also express spatial frequencies in terms of their corresponding wavelengths (or characteristic length scales) $\lambda_{xi} = 2\pi/k_{x_i}$ and $\lambda_{y_i} = 2\pi/k_{y_j}$. See Supporting Information for a complete derivation of Equation 1.

Even though the spectral solution derived by Wörman et al. (2006) used an orthogonal basis in the form $\sin(k_{xi}x)\, cos\,(k_{y_j}y)$, other functional forms can be used. For instance, Marklund and Wörman (2011) explored three different basis, including the periodic function $(h_{m,s})_{i,j}\ \sin(k_{xi}x + k_{y_i}y) + (h_{m,c})_{i,j}\ \cos(k_{xi}x + k_{y_i}y)$ used by Zijl (1999) where $h_{m,s}$ and $h_{m,c}$ are the Fourier coefficients of the sine and cosine components, respectively. Then, the spectral solution of the pressure head based on the previous orthogonal basis is given by (see Supporting Information for a complete derivation)

$$\begin{aligned} h(x, y, z) = \langle h \rangle + \sum_{j=1}^{N_y} \sum_{i=1}^{N_x} \frac{(\exp[zA] + \exp[(-2\varepsilon - z)A])}{1 + \exp(-2\varepsilon A)} ((h_{m,s})_{i,j}\ \ \sin(k_{xi}x + k_{y_j}y) \\ + (h_{m,c})_{i,j}\ \ \cos(k_{xi}x + k_{y_j}y)) \end{aligned} \tag{2}$$

Superposition can be used to further extend this condition to cases that better resemble exchange along a streambed. For example, we can include no-flow boundary conditions along lateral boundaries (e.g., $x - z$ plane for a channel parallel to the x axis) and a prescribed flow at depth $z = -\varepsilon$ to mimic the effect of regional groundwater upwelling or downwelling in bedform-driven hyporheic exchange (Gomez-Velez & Harvey, 2014).

Aside from the implicit assumptions of the conceptual model (e.g., homogeneous, isotropic, and rectangular domain), there is a critical source of uncertainty when using spectral solutions: the fit of the spectral function for the hydraulic head at the top boundary. In this study, we address this source of uncertainty, which depends on how well the spectral decomposition represents the hydraulic head at the top boundary ($h(x, y, z = 0) = H(x, y)$). Three components determine the implementation and quality of the spectral decomposition: (a) definition of the orthogonal basis, (b) definition of the pre-assigned frequency spectrum, and (c) regression technique to estimate the Fourier coefficients h_m.

First, the orthogonal basis should be flexible enough to capture the spatial structures observed in natural landscapes and streambeds. Wörman et al. (2006) show that the orthogonal basis used in Equation 1 provides 2–8 times lower relative error in the surface than the orthogonal basis used in Equation 2 with the same number of terms in the Fourier series. This result, however, is subjected to the definition of the pre-assigned frequency spectrum. The pre-assigned frequency spectrum defines the spatial frequencies k_{x_i} and k_{y_i} to be used in the Fourier series, and is bounded by the minimum spatial frequency (k_{min}) and the maximum spatial frequency (k_{max}) which are associated with the fundamental Fourier frequency and the Nyquist frequency, respectively (Crockett, 2019). In other words, the pre-assigned frequency spectrum is a sampling of spatial frequency pairs (k_{x_i}, k_{y_j}) in the interval $[k_{min}\ k_{max}]$. In practice, k_{min} is calculated with a wavelength equal to the domain size, and k_{max} is calculated with a wavelength equal to the spatial resolution of the hydraulic head boundary, which is constrained by the topography. The sampling of spatial frequencies within $[k_{min}\ k_{max}]$ is regulated by the number of sampled wavelengths (N) and the sampling method. For instance, Marklund and Wörman (2011) report that increasing the ratio between the number of Fourier coeffects and the number of data points from 23% to 97% decreases the average error from 3.8 to 1.7 m, in which if the ratio is 100% a perfect fit of the top boundary pressure head is attained. For large datasets, however, the definition of a large ratio, which is equivalent to large N, will significantly increase the computational burden and make impractical the estimation of the Fourier coefficients h_m. Hence, a proper sampling method with a reasonable number of frequencies needs to be adopted for the implementation of these spectral solutions.

2.2. The W06 Approach: Spectral Solution With a Single-Block Structured Frequency Spectrum

Wörman et al. (2006) present a widely used pre-assigned frequency spectrum based on a structured sampling of the spatial frequencies k_{x_i} and k_{y_i} within the interval $[k_{min}\ k_{max}]$:

$$k_{x_i} = a + bk_{max}(i/N_x)^c \;\; with \;\; i \in (1, 2, ..., N_x) \tag{3}$$

$$k_{y_i} = a + bk_{max}(i/N_y)^c \;\; with \;\; i \in (1, 2, ..., N_y)$$

where a is a lag controlling the smallest wavelength [L^{-1}], b is a scaling factor for the maximum wavelength [–], and c is a coefficient greater than 1 [–]. Following a notation like the one used in the numerical grid generation literature, we refer to this pre-assigned frequency spectrum as the *single-block structured frequency spectrum* (sbsFS; k_{sbsSF}), which is defined by the spatial frequency pairs

$$k_{sbsSF} = \left\{(k_{x_i}, k_{y_j}) : 1 \leq i \leq N_x, \;\; 1 \leq j \leq N_y\right\} \tag{4}$$

Once the orthogonal basis and the pre-assigned frequency spectrum are defined, the Fourier coefficients h_m are estimated by the least-square fitting of $h(x, y, z = 0)$, either from Equation 1 or Equation 2, to $H(x, y)$. The implementation of the spectral solution using Equation 1 with the pre-assigned frequency spectrum in Equation 4 is conducted using the codes "Spectop" and "Specvel" reported by Wörman et al. (2006). Through this study, the implementation of the spectral solution of groundwater flow equations by Wörman et al. (2006) is referred as W06, and the overview of its main steps is summarized in the left branch of Figure 1.

2.3. The P21 Approach: Spectral Solution With an Adaptive Unstructured Frequency Spectrum (auFS)

Here, we propose a new approach that focuses on the orthogonal basis used to derive Equation 2: $(h_{m,s})_{i,j}\ \sin(k_{xi}x + k_{y_i}y) + (h_{m,c})_{i,j}\ \cos(k_{xi}x + k_{y_i}y)$. This basis corresponds to the sum of cosines and sines of increasing frequency used in the two-dimensional Discrete Fourier Transform (DFT) (Kreyszig, 2014). We use the Fast Fourier Transform (FFT) algorithm to compute the DFT, representing the signal in the spatial frequency domain, and then, use a robust statistical technique to identify the significant frequencies in the power spectrum associated with the characteristic spatial scales of the hydraulic head at the top boundary. Once the statistically significant frequencies are identified, we incorporate those into the spectral solutions defined in Equation 2. The principle of this approach is to create a pre-assigned frequency spectrum by only exploring spatial frequency pairs (k_x, k_y) in areas that are not occurring by chance in the power spectrum based on a statistical significance level. We refer to this pre-assigned spectrum as the *adaptive unstructured frequency spectrum* (auFS; k_{auFS}) and it is defined as

$$k_{auFS} = \left\{sample^{[N]}\ (k_x, k_y) \sim U(k_x, k_y) | P_{\mathrm{DFT}}(k_x, k_y) > P_{\mathrm{DFT}_\alpha}(k_x, k_y)\right\} \tag{5}$$

where $sample^{[N]}\,(k_x, k_y)$ represents the random sample without repetition of N spatial frequency pairs, U is a uniform distribution of all possible combinations of $(k_x,\ k_y)$ pairs within the interval $[k_{min}\ k_{max}]$, $P_{\mathrm{DFT}}(k_x, k_y)$ is the spectral power for the pair (k_x, k_y), and $P_{\mathrm{DFT}_\alpha}(k_x, k_y)$ is the spectral power for the pair (k_x, k_y) with confidence level α (e.g., $\alpha = 0.05$ for a 5% confidence level). This pre-assigned frequency spectrum will assure the sampling of characteristic spatial scales that are found in quasiperiodic surfaces such as ridge-and-valley structures (Perron et al., 2008) and bedforms such as ripples and dunes (Hallet, 1990), and simultaneously will ignore spurious frequencies to optimize the representation of the hydraulic head at the top boundary. Note that a new form of Equation 2 needs to be introduced for the auFS frequency spectrum defined in of Equation 5 since the wavelength pairs are not necessarily symmetric such as those presented in the pre-assigned sbsFS frequency spectrum from Equation 3. In this case, the solution is recast as

$$\begin{aligned} h(x, y, z) = \langle h \rangle + \sum_{i=1}^{N} \frac{(\exp[zA] + \exp[(-2\varepsilon - \mathrm{z})A])}{1 + \exp(-2\varepsilon A)} \cdot \\ \cdot \left((h_{m,s})_i\ \ \sin(k_{xi}x + k_{y_i}y) + (h_{m,c})_i\ \ \cos(k_{xi}x + k_{y_i}y)\right) \end{aligned} \tag{6}$$

where k_{xi} and k_{y_i} represent a sampled spatial frequency pair from the definition in Equation 5, $i = 1, \cdots, N$.

We explain the estimation of the power spectrums $P_{\mathrm{DFT}}(k_x, k_y)$ and $P_{\mathrm{DFT}_\alpha}(k_x, k_y)$ in the following subsection. Once the significant spatial frequencies are identified, the next step is to estimate the Fourier coefficients $h_{m,s}$ and $h_{m,c}$ in Equation 6. The common approach is to use a least-square fitting approach, however, for large matrices, this approach can be highly ill-conditioned. For this reason, we implement the function "fitrlinear" in MATLAB including a ridge regularization with a support vector machine (SVM) learner. This regression approach is more robust to ill-conditioning than traditional Ordinary Least Squares (OLS) approaches, especially for large

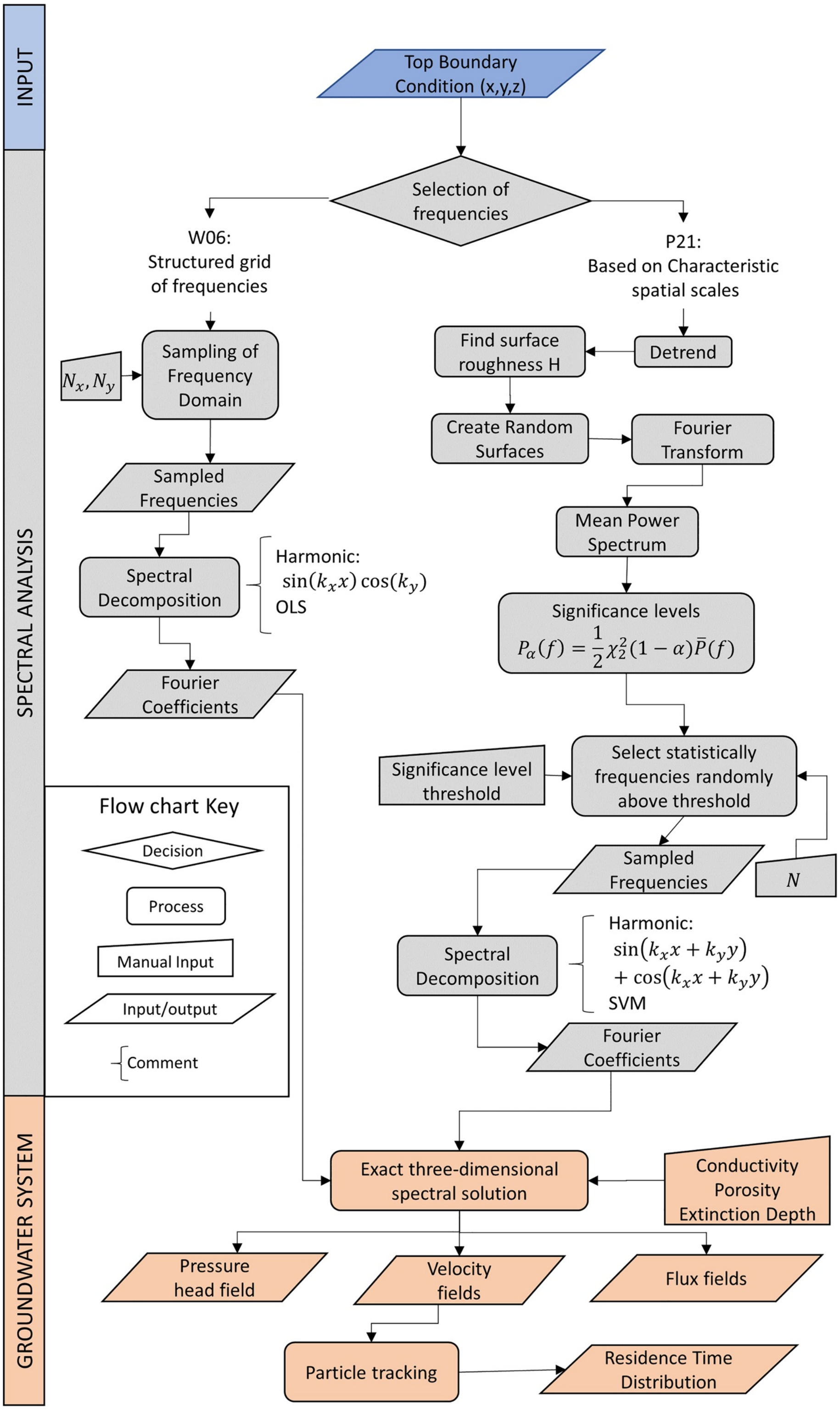

Figure 1. Flow chart describing the steps for the selection of dominant frequencies based on a spectral analysis in the solution of the groundwater flow system. The W06 is the spectral solution of groundwater flow equations by Wörman et al. (2006). The P21 (in reference to the contribution presented here) is the spectral solution based on the dominant frequencies.

matrices like the ones found in high-resolution Digital Elevation Models (DEMs) (Ho & Lin, 2012; Hoerl & Kennard, 1970). The condition number, defined as the ratio between the largest and smallest singular value of the matrix used in the regression analysis, is used as a diagnostic metric to assess the severity of ill-conditioning (Kutz, 2013). High values of the condition number are associated with matrices that are almost singular, leading to ill-conditioned problems that are prone to large numerical errors.

2.3.1. Identification of Dominant Frequencies

We adopt the approach presented by Perron et al. (2008) to identify dominant frequencies in the power spectrum, and consecutively define the auFS frequency spectrum for the spectral solution presented in Equation 6. This procedure comprises five main steps, which we briefly describe here:

2.3.1.1. Step 1. Calculate the Top Boundary DFT

The 2D Discrete Fourier Transform (DFT) for the top boundary hydraulic head, $h(x, y, z = 0) = H(x, y)$, is obtained by discretizing the frequency domain into M_x columns and M_y rows, evenly spaced with intervals of size Δx and Δy, as

$$\mathrm{Z}(k_x, k_y) = \sum_{m=0}^{k_x-1} \sum_{n=0}^{k_y-1} H(m\Delta x, n\Delta y) e^{-2\pi i\left(\frac{k_x m}{M_x} + \frac{k_y m}{M_y}\right)} \tag{7}$$

where m and n are indices in the z array such as $x = m\Delta x$ and $y = n\Delta y$, the two orthogonal frequency components are defined by $f_x = \frac{k_x}{M_x \Delta x}$ and $f_y = \frac{k_y}{M_y \Delta y}$, and the ranges of the spatial frequencies are $-M_x/2 \leq k_x \leq M_x/2 - 1$ and $-M_y/2 - 1 \leq k_y \leq M_y/2$.

The DFT is calculated using the FFT algorithm with the following considerations. First, because the Fourier transform assumes a stationary signal within the sampled interval, we detrend the signal with a linear function in the *x*-*y* plane to guarantee a constant mean in the domain. Second, the Fourier transform assumes periodicity, which is not necessarily true for topography or hydraulic head surfaces. In fact, violating this assumption can result in significant spectral leakage, where spectral power is assigned to multiple spurious frequencies to describe edge discontinuities (Percival et al., 1993). To reduce the spectral leakage, we multiplied the detrended signal by the *Hann* window function, which is represented for a raised cosine with a maximum in the center and decreases smoothly to zero at the edges (Mallat, 2008). Finally, the power spectrum is normalized to consider the change in variance due to the window function.

2.3.1.2. Step 2. Obtain the 2D Power Spectrum

The power spectrum P_{DFT} (with units of amplitude squared per frequency squared) is obtained from the results of the DFT approximation from Step 1

$$P_{\mathrm{DFT}}(k_x, k_y) = \frac{1}{M_x^2 M_y^2} |\mathrm{Z}(k_x, k_y)|^2 \tag{8}$$

The power spectrum, also known as the DFT periodogram, provides a measure of how much of the signal's variance is explained by a spatial frequency pair (k_x, k_y).

2.3.1.3. Step 3. Calculate the 1D Power Spectrum

In this step, the 2D power spectrum from Step 2 is transformed into a 1D power spectrum. The 1D spectrum is defined as the relationship between DFT's mean-squared amplitude and radial spatial frequency $\sqrt{k_x^2 + k_y^2}$. Natural landscapes are characterized by decreasing spectral power as frequency increases with a high-frequency roll-off where a drastic change in the slope of the 1D power spectrum occurs. We identify the roll-off frequency as the radial spatial frequency that separates the "linear" behavior of the 1D spectrum. Briefly, the slope change is identified with a least-squares regression procedure between radial spatial frequency and the 1D power spectra over a varying interval, beginning with the lowest frequency and subsequently increasing the range in the regression. Then, the roll-off frequency is identified as the point with a higher regression line slope after the goodness of fit (as measured by the coefficient of determination) reaches a plateau.

2.3.1.4. *Step 4. Estimate the Background Spectrum*

The background spectrum $\bar{P}(k_x, k_y)$ represents a 1D power spectrum with the same statistics of the original signal but without characteristic spatial scales. This spectrum can be estimated from the power spectrum of the original signal by using the binning approach proposed by Perron et al. (2008) or with the generation of a series of random signals that preserve the statistics of the original signal but lack characteristic scales. Because binning is prone to bias due to high peaks in the observed spectrum, we use the latter approach, where $\bar{P}(k_x, k_y)$ is estimated from the average of the power spectra from a large number random signal surfaces (i.e., random hydraulic head surfaces) sharing the same statistical properties than the original signal (i.e., the hydraulic head boundary condition, dictated by topography) but without concentration of variance at any spatial frequency band (i.e., without a dominant characteristic scale). Here, we use the diamond square algorithm (Fournier et al., 1982) to generate 1,000 random surfaces. This algorithm is commonly used to generate random fractal surfaces, where the slope of their power spectrum is controlled by a single parameter S. This parameter is associated with the surface roughness and varies from 0 (roughest) to 1 (smoothest). The parameter S is found in advance with a least-square fit to match the 1D power spectra from the random signal surfaces and the original signal for frequencies higher than the roll-off frequency defined in Step 3.

2.3.1.5. *Step 5. Identify Statistically Significant Spatial Frequencies*

Our objective is to find the "confidence level at which we can reject the null hypothesis that an observed periodic signal has occurred by chance in a random surface," where the confidence level is defined as "the probability that the spectrum of a random surface will exceed the background spectrum by the observed amount at that frequency." Assuming that the Fourier coefficients are random, normally distributed variables, the spectral power at a given spatial frequency will be chi-squared (χ^2) distributed with two degrees of freedom, and the spectral power corresponding to a confidence level α is (Percival et al., 1993)

$$P_{\mathrm{DFT}_\alpha}(k_x, k_y) = \frac{1}{2}\chi_2^2(1-\alpha)\bar{P}(k_x, k_y) \tag{9}$$

where $\bar{P}(k_x, k_y)$ is the background spectrum of the top boundary hydraulic head surface (estimated in Step 4) and $\chi_2^2(1-\alpha)$ is the value at which the χ_2^2 cumulative distribution function with 2 degrees of freedom equals $1-\alpha$.

The *adaptive unstructured frequency spectrum* (auFS) in Equation 5 is defined once $P_{\mathrm{DFT}}(k_x, k_y)$ and $P_{\mathrm{DFT}_\alpha}(k_x, k_y)$ are obtained from the previous steps. Given the symmetry of the power spectrum P_{DFT}, we only explore the spatial frequencies in the first and fourth cartesian quadrants of the $k_x - k_y$ plane. Also, because the hydraulic head surface was detrended (Step 1), we include additional spatial frequencies into the pre-assigned auFS spectrum to capture the regional slopes in the x and y directions. These regional trends can be captured by spatial frequencies with wavelength of the order of 2–3 times the length of the modeling domain. If the dominant frequencies are clustered in the pre-assigned frequency spectrum these are less likely to be "false positives" (Perron et al., 2008), and, depending on the surface characteristics, dominant frequencies might be quite small (e.g., representing quasiperiodic ridge-and-valley structures). Finally, it is recommended to interpolate the final $P_{\mathrm{DFT}_\alpha}(k_x, k_y)$ with smaller frequency increments than those provided by the DFT in order to guarantee a larger sampling space on lower frequencies by Equation 5.

The code used to identify the dominant frequencies and the implementation of the corresponding spectral solutions is available in a public GitHub repository (see the Acknowledgments and Data Availability Sections) as MATLAB codes "SS_DomFreq", "SS_Top", and "SS_Vel," which are built upon the codes provided by Wörman et al. (2006) and Perron et al. (2008). Hereinafter, the spectral solution based on the dominant frequencies is referred as P21, in reference to the contribution presented here, and the overview of its main steps is summarized in the right branch of Figure 1.

3. Application to Testbeds and Benchmark Data

We use three different testbeds to evaluate the strengths and limitations of the proposed approach, and how it compares with previous ones. The testbeds include the following systems (a) a synthetic periodic basin, (b) synthetic sandy bedforms, and (c) a natural mountainous basin. For each system, we modeled groundwater flow and advective transport with three different approaches: (a) W06, (b) P21, and (c) reference. W06 is the standard approach using Equation 1 with the pre-assigned sbsFS spectrum in Equation 4. P21, the approach proposed in this work, uses Equation 6 with the pre-assigned auFS spectrum with dominant frequencies presented in Equation 5. The reference approach uses exact analytical or numerical solutions to evaluate the performance of W06 and P21.

Specifically, the reference for the synthetic periodic basin is based on the exact analytical solution derived by J. Z. Wang et al. (2016), and the reference for the synthetic sandy bedforms and the natural mountainous basin is based on a high-resolution finite element numerical solution implemented in COMSOL Multiphysics. To have a fair comparison, the same number of Fourier coefficients are used for both approaches.

The performance of the approaches will be assessed in terms of how well the top boundary hydraulic head is reproduced and how the spatial distribution of recharge and discharge areas, fluxes, and RTD are captured with respect to the reference approach. The RTDs are obtained with a particle-tracking approach based on a fourth-order Runge-Kutta integration method with 10,000 particles randomly released from the recharge areas at the top boundary of the study domain.

3.1. Synthetic Periodic Basin

Here, we mimic a periodic and multiscale regional groundwater flow systems with a 3D extension of the classic 2D Tothian basin (Toth, 1963). The topographic surface, which also corresponds to the hydraulic head at the top boundary, is defined as

$$z(x, y) = h(x, y, z = 0) = z_0 + H_{Rx} cos\left(\frac{\pi}{L_x}x\right) + H_{L_x}\ \cos\left(\frac{m_L \pi x}{L_x}\right) + H_{L_y}\ \cos\left(\frac{n_L \pi y}{L_y}\right) \tag{10}$$

where z_0 is the mean elevation, H_{Rx} is the amplitude of the regional terrain elevation in the x-direction, and H_{L_x} and H_{L_y} are the amplitudes of the local terrain elevation in x-direction and y-direction, respectively. The parameters m_L and n_L determine the frequencies of local undulations in x-direction and y-direction, respectively. L_x and L_y are characteristic length scales in x-direction and y-direction, respectively. The exact analytical solution for the hydraulic head field in this case is given by J. Z. Wang et al. (2016):

$$\begin{aligned} h(x, y, z) = z_0 &+ \frac{H_{R_x}\ \cos\left(\frac{\pi x}{L_x}\right)\cosh\ \left(\frac{\pi}{L_x}(z-\varepsilon)\right)}{\cosh\ \left(\frac{\pi}{L_x}\varepsilon\right)} + \frac{H_{L_x}\ \cos\ \left(\frac{m\pi x}{L_x}\right)\cosh\ \left(\frac{m\pi}{L_x}(z-\varepsilon)\right)}{\cosh\ \left(\frac{m\pi}{L_x}\varepsilon\right)} \\ &+ \frac{H_{L_y}\ \cos\ \left(\frac{n\pi y}{L_y}\right)\cosh\ \left(\frac{n\pi}{L_x}(z-\varepsilon)\right)}{\cosh\ \left(\frac{n\pi}{L_x}\varepsilon\right)} \end{aligned} \tag{11}$$

We select the following parameters as a test case: $z_0 = 400$ m, $H_{Rx} = 100$ m, $H_{L_x} = 50$ m, $H_{L_y} = 5m_L$, $m_L = 7$, $n_L = 20$, $L_x = 90$ km and $L_y = 90$ km. The subsurface hydraulic conductivity and porosity are assumed to be $3.2 \cdot 10^{-6}$ m/s and 0.3, respectively—consistent with similar modeling examples (Caruso et al., 2016; Heath, 1983). To mimic data obtained as a DEM, we discretize the continuous function in Equation 10 in a matrix with uniform resolution of 100 m in the domain $x \in [0,\ \ 90]$ km and $y \in [0,\ \ 90]$ km. For a better visualization of spatial patterns in the top boundary pressure head and groundwater fluxes, the outputs derived from the spectral solutions will be analyzed on the domain $x \in [30,\ \ 60]$ km and $y \in [30,\ \ 60]$.

3.2. Synthetic Periodic Bedforms

The second test case focuses on bedform-induced hyporheic exchange. We use the following expression to approximate the topography of natural quasi-periodic bedforms (Rubin & Carter, 2005; Chen et al., 2018):

$$z_i^{surf} = \frac{\eta \lambda_L}{l}\left(7.5 - 6\ \sin\left(\frac{\pi l}{50\lambda_L}m_i\right) - 1.5\ \sin\left(\frac{\pi l}{25\lambda_L}m_i\right)\right) \tag{12}$$

where m_i is given by

$$m_i = x - \frac{\lambda_L \varphi_i^{bf}}{360} - A_i^f\ \sin\left(\frac{2\pi}{\lambda_T}y + \frac{2\pi}{360}\alpha_i\right) - A_i^s\ \sin\left(\frac{4\pi}{\lambda_T}y + \frac{2\pi}{360}\beta_i\right) \tag{13}$$

$$z_H(x, y) = \max\ \left(z_i^{surf}\right)\ \ with\ \ i = 1,\ \ 2 \tag{14}$$

and $x, y \in (-\frac{l}{2}, \frac{l}{2})$ are cartesian coordinates, with l being the length of the repeating unit block. This geomorphic model combines two periodic functions to approximate the shape of quasi-periodic bedforms. These periodic functions denoted by subscript i ($i = 1, 2$) have planform amplitudes A_i^f and A_i^s; bedform phase (in degrees) φ_i^{bf} is for controlling the placement of the bedform within the unit block; the mean steepness (height-to-wavelength ratio) is η. λ_L and λ_T are the longitudinal and transverse wavelengths of the bedform, respectively; α_i and β_i are the phases (or phase shift for the crest placement) of the first and second planform sinuosity of each bedform.

Our test case uses the following parameters to resemble aqueous sandy bedforms (Rubin & Carter, 2005): $\eta = 0.8$, $\lambda_L = 75$, $l = 100$ cm, $\varphi_1^{bf} = 0°$, $\varphi_2^{bf} = 180°$, $A_1^f = A_2^f = 13$, $\lambda_T = 50$, $\alpha_1 = \alpha_2 = 0°$, $A_1^s = A_2^s = 3$, $\beta_1 = \beta_2 = 90°$, and a slope S_0 of 0.05% is superimposed in the x-direction.

The hydraulic head at the sediment-water interface (SWI), which drives hyporheic exchange, includes the combined effect of both hydrostatic and dynamic pressure variations. For simplicity, and similar to previous contributions (Singh et al., 2019, 2020; Stonedahl et al., 2010, 2013; Wörman et al., 2006, 2007; Wu et al., 2018, 2020), we use the pumping model (Elliott & Brooks, 1997b), which assumes that the dynamic head follows the bed topography with a phase shift, and amplitude that depends on the channel hydraulics:

$$h(x, y, z = 0) = H(x, y) + h_m \frac{\left[Z\left(x + \frac{\lambda_L}{4}, y\right) - \bar{Z}\right]}{H_B/2} - S_0 x \tag{15}$$

with

$$h_m = \frac{0.28V^2}{2g}\begin{cases} \left(\dfrac{(H_B/d)}{0.34}\right)^{\frac{3}{8}} & for \quad \dfrac{H_B}{d} \le 0.34 \\ \left(\dfrac{(H_B/d)}{0.34}\right)^{\frac{3}{2}} & for \quad \dfrac{H_B}{d} \ge 0.34 \end{cases} \tag{16}$$

Where H_B is the bedform height, d is average flow depth, $\bar{Z}$ is the mean surface elevation, and $H(x, y)$ is the static head which is assumed as the average flow depth d. Our test case uses an average channel velocity of 0.12 m/s and flow depth of 0.5 m. The hydraulic conductivity and porosity used in the sandy bedforms are 9.8067×10^{-4} m/s and 0.3, respectively—similar to Chen et al., (2018). In this case, the reference solution is approximated with a finite element numerical solution. COMSOL Multiphysics was used for the implementation with ~7.3 million elements over a domain of $3\lambda_L \times 3\lambda_T$. This fine discretization was needed to achieve a mesh-independent solution that captures the small-scale details of this multiscale flow system.

3.3. Natural Mountainous Watershed

We use the Rio Hondo watershed to explore multiscale groundwater flow in a real system. Rio Hondo is a mountain watershed with steep and complex topography located in northern New Mexico, USA. We use a Digital Elevation Model (DEM) with a 1/3 arcsec (~10 m) horizontal resolution from the U.S. Geological Survey's National Elevation Data Set. In this case, the DEM covers a rectangular area of 365 km^2, which includes the Rio Hondo watershed with a drainage area of 185 km^2. The outlet of the delineated watershed is located 3 km downstream from the USGS streamflow gauge Arroyo Hondo at Arroyo Hondo (USGS code 08268500). We resampled the DEM to 70 m, following the findings of Marklund and Wörman (2011), who suggested this as an optimal resolution for the top boundary condition in spectral solutions for the study of basin-scale groundwater flow. Their argument is that the resampling is needed to represent undulations of water table that are smoother than the real topography (Wolock & Price, 1994). The study of the Rio Hondo basin will allow us to assess the ability of the proposed methodology to detect dominant frequencies in the spectral analysis for characterizing the landscapes where the characteristic spatial scales are not as simple as those in the synthetic basins and bedforms. Here, we used a hydraulic conductivity and porosity equal to 10^{-4} m/s and 0.3, respectively. Like the bedform case, we use a finite element method to estimate the reference solution. The model was implemented in COMSOL Multiphysics and solved with a mesh of approximated 14.2 million elements.

4. Results

In this section, we evaluate the performance of W06 and P21 for representing the hydraulic head at the top boundary (Section 4.1), groundwater fluxes (Section 4.2), and RTDs (Section 4.3) with respect to the benchmark data to each testbed. For the use of W06 and P21, we used 784 (28^2) Fourier coefficients for both Tothian basin and

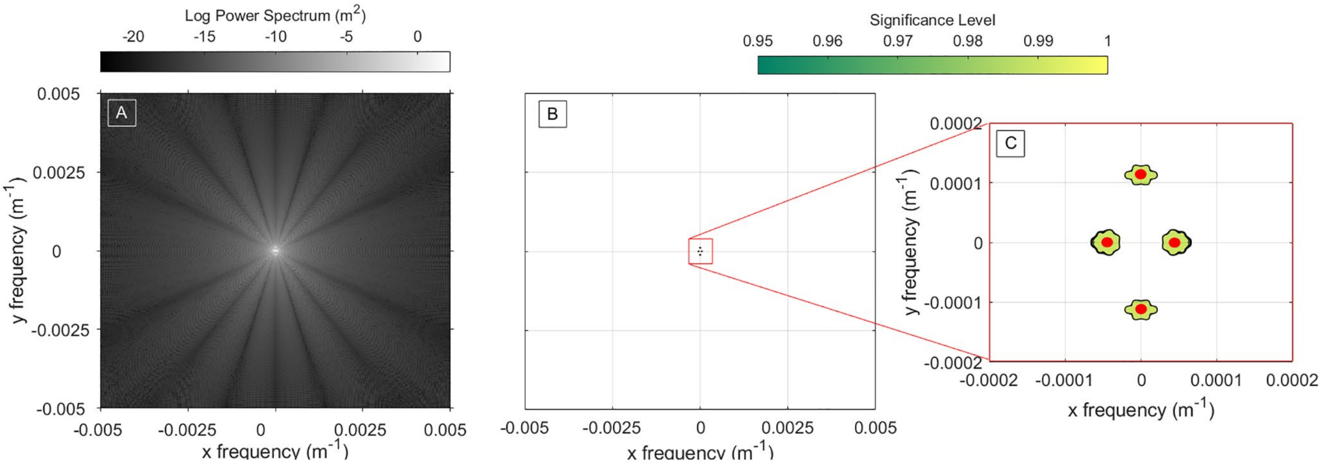

Figure 2. (a) Power Spectrum obtained from the Discrete Fourier Transform (DFT) of the 3D Tothian basin. (b) Spatial frequencies with more than a 95% significance level based on Perron et al. (2008). (c) Zoom-in of the dominant spatial frequencies for better visualization. The red points on panel (c) represent the location of the a priori frequencies defined in Equation 10.

synthetic bedforms. For the case of the Rio Hondo watershed, which has a more complex representation of the top boundary hydraulic head, we used 4,900 (70^2) Fourier coefficients. For the Tothian basin and the synthetic bedforms, we used P21 with a 95% significance level. For the Rio Hondo watershed, where the dominant frequencies are more randomly distributed in the power spectrum, we used a significance level of 0%, equivalent to a random sampling of the 2D power spectrum. Section 4.4 will provide a robust evaluation of the number of Fourier coefficients and significance levels in using P21 for reconstructing the top boundary hydraulic head and the groundwater fluxes (discharge and recharge) for each case study.

4.1. Hydraulic Head at the Top Boundary

In this subsection, we evaluate the ability of the W06 and P21 approaches to reproduce the hydraulic head at the top boundary, that is, their ability to reproduce the main driver for groundwater flow. The synthetic periodic basin, represented by a Tothian domain, is ideal to assess the performance of Equation 5 in selecting the dominant frequencies, which are known a priori. In this case, we imposed dominant frequencies for the local undulations in y-direction and x-direction of 11×10^{-5} and 3.8×10^{-5} m^{-1}, respectively, and a regional undulation of 5.5×10^{-6} m^{-1} in the x-direction (see Equation 10). Our approach identifies statistically significant frequencies (as defined by a significance level larger than 95%) that tightly enclose the true values (see Figure 2c). The dominant frequency associated with the regional undulation in the x-direction, a wavelength of approximately 180 km, is not, captured because the domain used in this example is limited to a square of 90 km by 90 km, which is much smaller than the length of this regional undulation.

Like the Tothian case, the quasi-periodic structure of the synthetic bedforms results in well-organized and focused dominant frequencies in the 2D power spectrum (see Figure S1 in Supporting Information S1). On the other hand, the power spectrum of the Rio Hondo watershed exhibits a less organized and more random pattern (see Figure S2 in Supporting Information S1 for an example of the power spectrum for spatial frequencies with more than a 50% significance level) which is characteristic of a landscape with multiple important spatial scales. This random pattern suggests that dominant frequencies with high significance levels (e.g., 95%) are unlikely to capture all the multiple spatial scales required to reproduce the top boundary hydraulic head described by the landscape of the Rio Hondo watershed. With this in mind, we found that a significance level of 0%, which is equivalent to a random sampling of the 2D power spectrum, provides the best depiction of the Rio Hondo landscape. A detailed analysis of the influence of significant levels in the use of P21 in the three case studies is presented in Section 4.4.

From a numerical perspective, we found that for all our simulations, the linear regression with a support vector machine learner with ridge regulation overcomes the ill-conditioned nature of this problem, providing more stable Fourier coefficients estimates than the Ordinary Least Squares regression for both W06 and P21. In general, the P21 approach results in condition numbers that are lower than the W06 approach (see Table 1), demonstrating the improved stability of the regression analysis.

Table 1

Statistics Showing the Comparison Between W06 and P21 With Respect to the Reference Model

	Tothian			Sandy bedforms			Rio Hondo watershed		
	Ref	W06	P21	Ref	W06	P21	Ref	W06	P21
Conditional Number		8.4 E+16	1.0 E+16		1.4 E+16	2.9 E+07		3.83 E+16	2.02 E+15
Z MAPE(%)	–	1.5	6.74E−05	–	0.0053	0.0016	–	1.73	1.52
Z MAPE(%) in Q+ area	–	1.6	7.07E−05	–	0.0054	0.0020	–	1.79	1.61
Z MAPE(%) in Q- area	–	1.4	6.43E−05	–	0.0052	0.0012	–	1.79	1.60
$Q+ (\frac{m^3}{s})$	10.8	12.2	10.5	1.00E−6	8.50E−7	1.04E−6	2,581	2,300	2,585
$Q + RE(\%)$	–	−12.5	2.4	–	15.6	−3.4	–	10.9	−0.2
$Q\text{-}(\frac{m^3}{s})$	9.8	10.5	9.5	−9.81E−7	−7.80E−7	−1.00E−6	−2428	−2137	−2506
Q-RE(%)	–	−7.7	2.7	–	20.58	−2.54	–	12.0	−3.2

Note. Z MAPE (%): Mean Absolute Percentage Error in the estimation of the water table. The Z MAPE (%) in Q+ area (or Q-area): are Z MAPE (%) calculated within the discharge area Q+ area (or recharge area Q-) defined by the reference model (Ref). Q+ $(\frac{m^3}{s})$ Flow Magnitude within the discharge area defined within the same model, Q- $(\frac{m^3}{s})$ Flow Magnitude within the recharge area defined within the same model. Q + RE(%) (or Q- RE(%)) shows the Relative Error in discharge (or recharge) of each model with respect to the reference model.

From the perspective of reproducing the top boundary condition, we also see a significant improvement by using the P21 approach. The adequacy in the estimation of the Fourier coefficients in W06 and P21 can be easily assessed based on a proper decay of the probability density of the amplitude-to-wavelength ratio ($|\boldsymbol{h_m}|/\lambda$) with the respective pre-assigned spatial frequency spectrum (see Figure 3 for the Tothian basin and Figures S3 and S4 in Supporting Information S1 for the bedforms and the Rio Hondo watershed, respectively). As expected, the pre-assigned auFS spectrum in P21 selects frequencies that are clustered near the dominant frequencies maintaining a proper power spectrum decay (e.g., Figure 3b). Visual inspection suggests that W06 and P21 perform

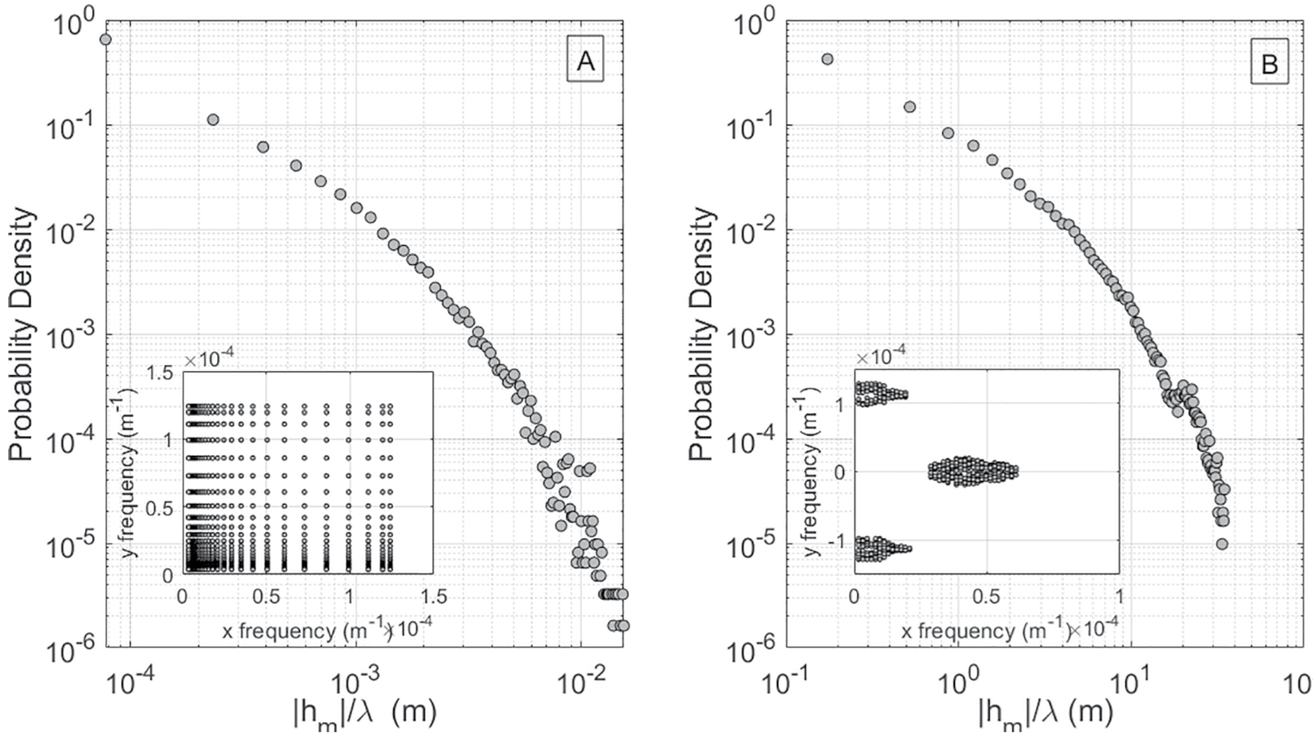

Figure 3. Probability density of the amplitude-to-wavelength ratio ($|h_m|/\lambda$) of the 3D Tothian basin based on the (a) pre-assigned sbsFS spectrum used in W06 and (b) auFS spectrum based on dominant frequencies used in P21. The embedded panels show the selected spatial frequencies sampled in both approaches.

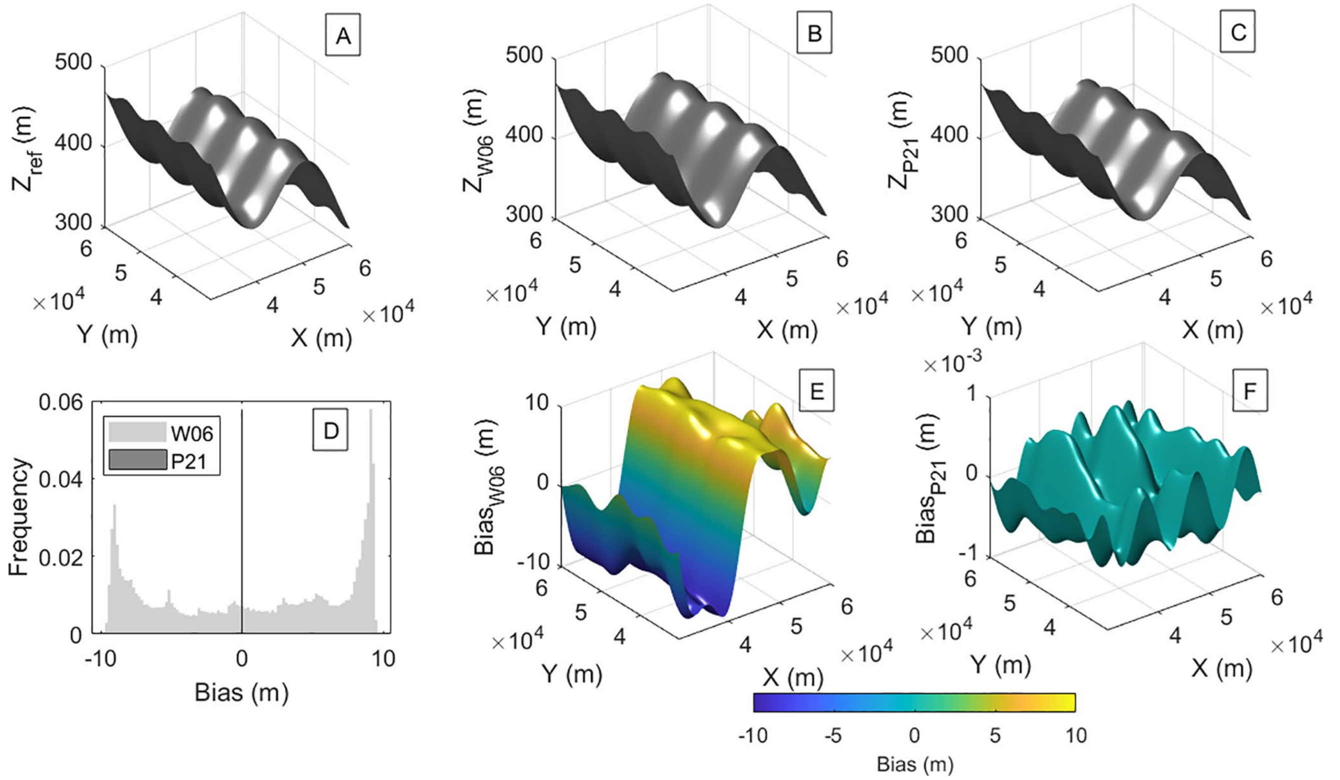

Figure 4. Reconstruction of the top boundary hydraulic head (panel a) in the 3D Tothian basin using W06 (panel b) and P21 (panel c) with their respective biases calculated as $Z_{W06\,(or\,P21)} - Z_{ref}$ (panels d–f).

similarly in the approximation of the top boundary surface (see Figures 4a–4c); however, a detailed inspection shows that the Mean Absolute Percentage Error (MAPE) in the estimation of the hydraulic head surface with P21 (MAPE of 6.74E−5%) is orders of magnitude smaller than with the W06 approach (MAPE of 1.5%) (Table 1). The priori identification of statistically significant spatial frequencies successfully captures areas in the spectrum surrounding the true spatial frequencies defined for the Tothian basin. Regarding the other two cases, the MAPE for the Sandy bedforms hydraulic head is reduced by a factor of 3.3 when the P21 is used (0.0053% for W06% and 0.0016% for P21). For the Rio Hondo watershed, the MAPE for hydraulic head is reduced by a factor of 1.1 (1.73% for W06% and 1.52% for P21). The spatial frequencies sampled in P21 for the Tothian case (Figure 3) and bedform (Figure S1 in Supporting Information S1) are clustered around the true spatial frequencies representing the periodic and quasi-periodic structure found on both surfaces. On the contrary, the spatial frequencies sampled for the Rio Hondo watershed are significantly more dispersed over the spatial frequency domain (see Figure S2 in Supporting Information S1). While the improvements in the errors are less striking for the bedforms and Rio Hondo watershed, their implication for the estimation of fluxes and residence times is amplified, given the strong dependance of these metrics on the gradient of the hydraulic head surface. More details in the following subsections.

4.2. Groundwater Fluxes

The flux perpendicular to the top boundary of the domain $q_{top} = \boldsymbol{n} \cdot \boldsymbol{q}$, with $\boldsymbol{q}$ being the Darcy flux vector and $\boldsymbol{n}$ being an outward normal vector, is used to identify recharge ($q_{top} < 0$) and discharge ($q_{top} > 0$) areas. In the case of our spectral solutions, which have a horizontal top boundary, this corresponds to the vertical component of the Darcy flux vector q_z. We compare the W06 and P21 approaches based on their ability to reproduce the spatial variability in fluxes and their cumulative mass.

The P21 approach outperforms W06 for the three test cases. We found that W06 provides an average error of the discharge (recharge) flow of −12.5% (−7.7%) (Table 1 and Figure 5) for the Tothian basin. By contrast, the results

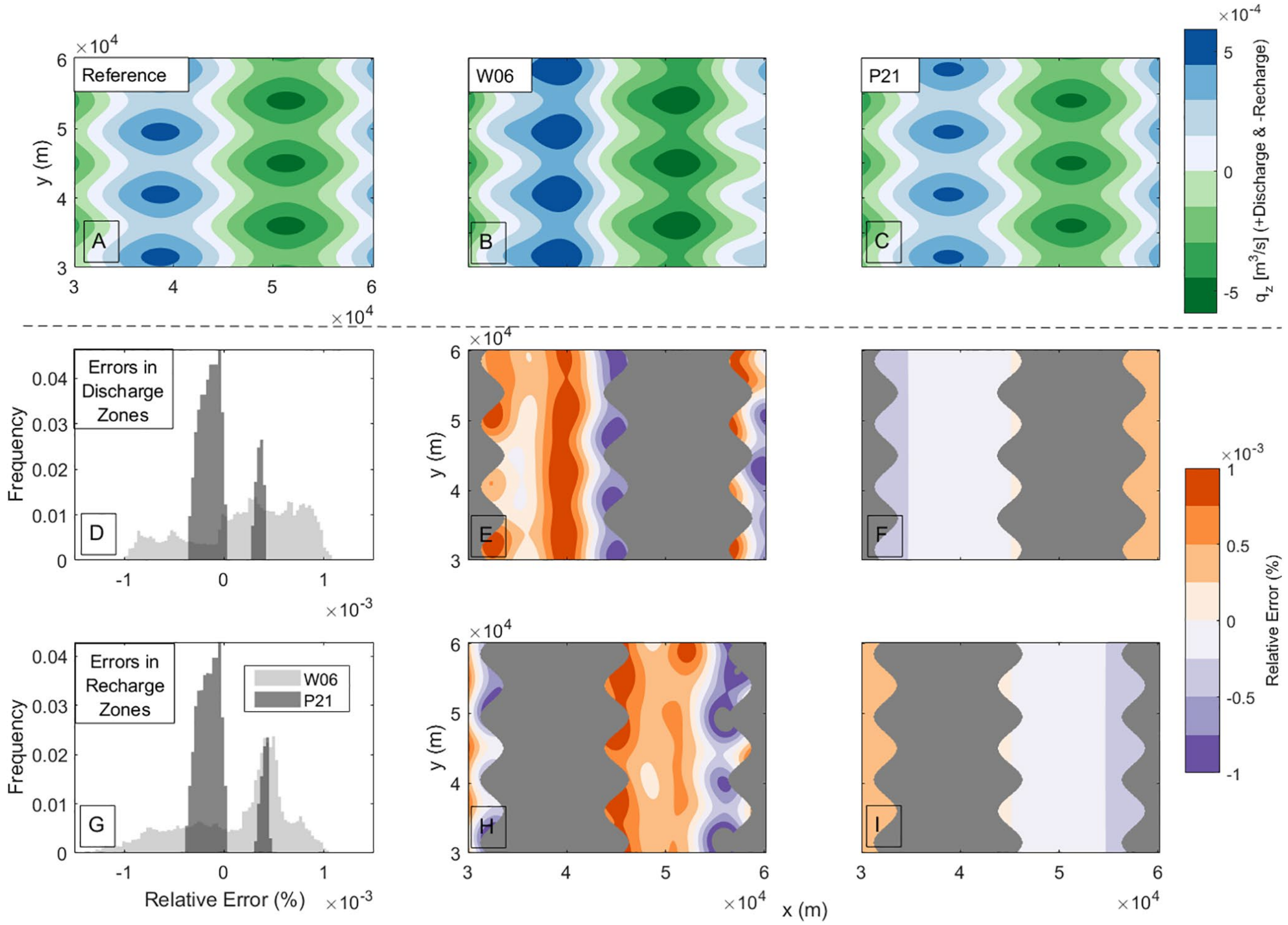

Figure 5. Fluxes in the *z*-direction on the top layer ($z = 0$) for the 3D Tothian Basin based on the reference model (panel a), W06 (panel b), and P21 (panel c). The relative errors with respect to the reference model for W06 and P21 are shown in the discharge (panels e and f) and recharge (panels h and i) areas. The histogram of relative errors in the discharge and recharge zones are shown in panels d and g, respectively. The relative errors in the discharge or recharge zones are calculated as the ratio of the difference in fluxes between the spectral solution and the reference model over the total discharge or recharge flux estimated over the reference model.

with P21 provide discharge (recharge) errors of 2.4% (2.7%). For the sandy bedforms (Table 1 and Figure 6), we found a much higher bias in the recharge and discharge fluxes with the W06 approach, with a discharge (recharge) error of 15.6% (20.58%) for W06 and −3.4% (−2.54%) for P21.

Regarding the results for groundwater fluxes in the Rio Hondo watershed, we found that P21 provides discharge (recharge) errors of −0.2% (−3.2%), improving the results from the W06 approach, which has a discharge (recharge) error of 10.9% (12.0%) (Table 1). However, despite the notable difference in discharge (recharge) errors between W06 and P21, both approaches present coarse representations of the spatial distribution of discharge and recharge areas with respect to the reference model (Figure 7). These large differences in the spatial representations of fluxes are caused by the spectral decomposition's inability to capture sharp increases in high-gradient areas such as the landscape ridges and river network. In other words, the spectral approximation of the hydraulic head at the top boundary is smoother than the water table used as a boundary condition for the reference numerical model.

These results demonstrate that small biases in the top boundary hydraulic head can have significant impacts on discharge and recharge fluxes. In particular, the P21 approach better captures the spatial variability of the fluxes, which are characterized by sharp transitions, especially in the case of the Tothian basin and bedforms.

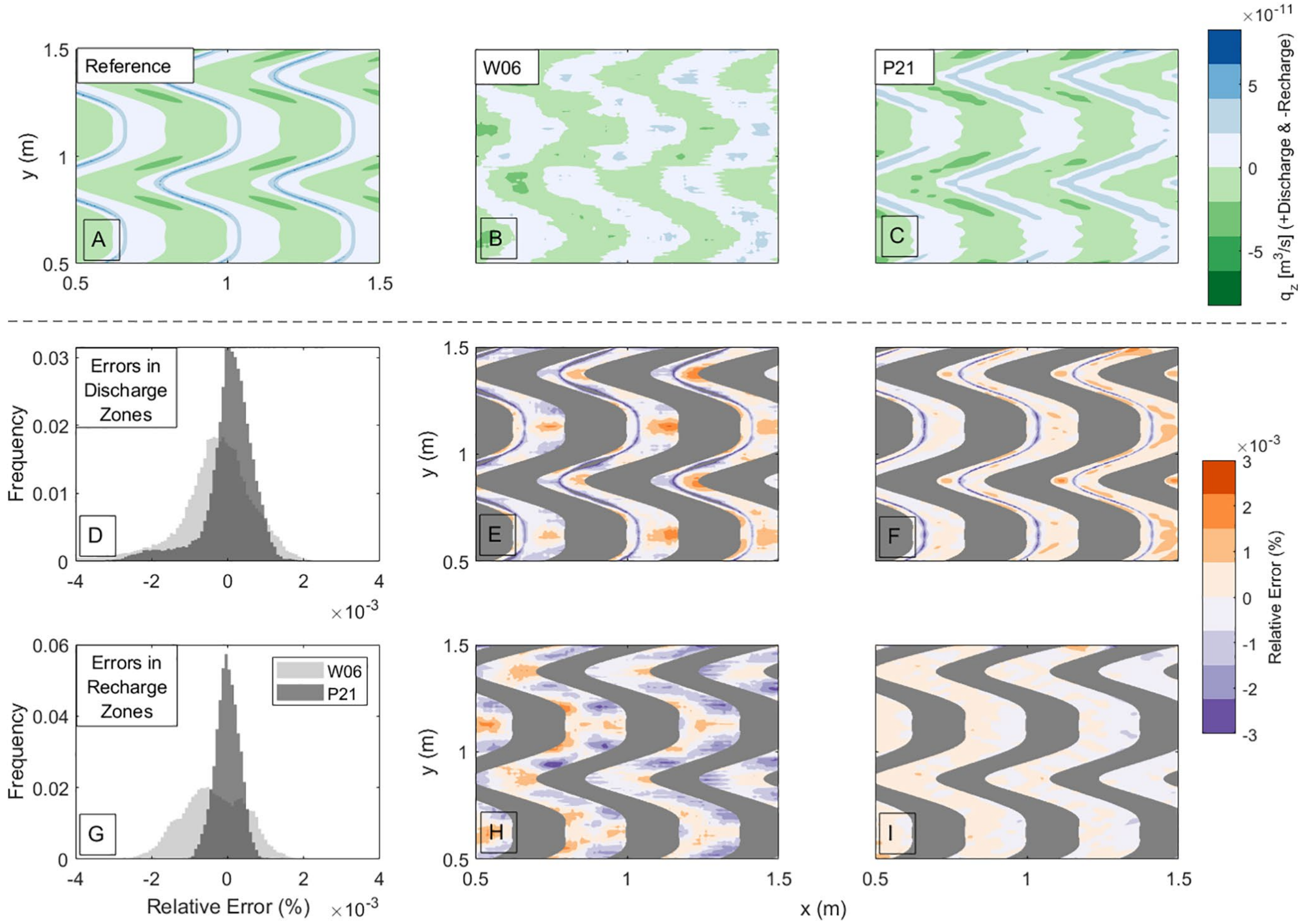

Figure 6. Fluxes in the z-direction on the top layer ($z = 0$) for the sandy bedforms based on the reference model (panel a), W06 (panel b), and P21 (panel c). The relative errors with respect to the reference model for W06 and P21 are shown in the discharge (panels e and f) and recharge (panels h and i) areas. The histogram of relative errors in the discharge and recharge zones are shown in panels d and g, respectively. The relative errors in the discharge or recharge zones are calculated as the ratio of the difference in fluxes between the spectral solution and the reference model over the total discharge or recharge flux estimated over the reference model.

4.3. Residence Time Distributions

Using the flow field from the spectral and reference solutions, we estimated the RTDs of the water exchanged by the three testbeds with a particle tracking algorithm (see Figure S7 in Supporting Information S1 for an example of the obtained flow paths). RTDs encapsulate the transport characteristics of groundwater systems and represent fundamental metrics to characterize biogeochemical potential (Boano et al., 2010; Gomez et al., 2012; Gomez-Velez et al., 2017; Zarnetske et al., 2011, 2012) and the interpret environmental and artificial tracers (Frisbee et al., 2011; Gomez & Wilson, 2013).

The Tothian basin's RTD obtained with the W06 and P21 approaches match the reference model (see left column in Figure 8). This result contrasts with the significant biases observed in the recharge and discharge fluxes. Although both approaches have significant differences in their estimates of flux magnitude at the recharge and discharge areas, the overall structure of the flow field is controlled by the regional fluctuations in the water table (see left column in Figure S7 in Supporting Information S1), which is consistent with a unimodal RTD and well-represented by both spectral solutions.

For the sandy bedforms, we found that the RTD for P21 resembles the RTDs derived by the reference approach (see panels b and e in Figure 8), which is consistent with the accurate representation of fluxes in P21 (see Figure 6). On the other hand, the RTD from the W06 approach is characterized by older water in comparison with the other two approaches. This bias can be explained by the inability of the W06 approach to capture small-scale hydraulic head fluctuations (see Figure 6), which control the shorter residence times. Note that the RTDs in

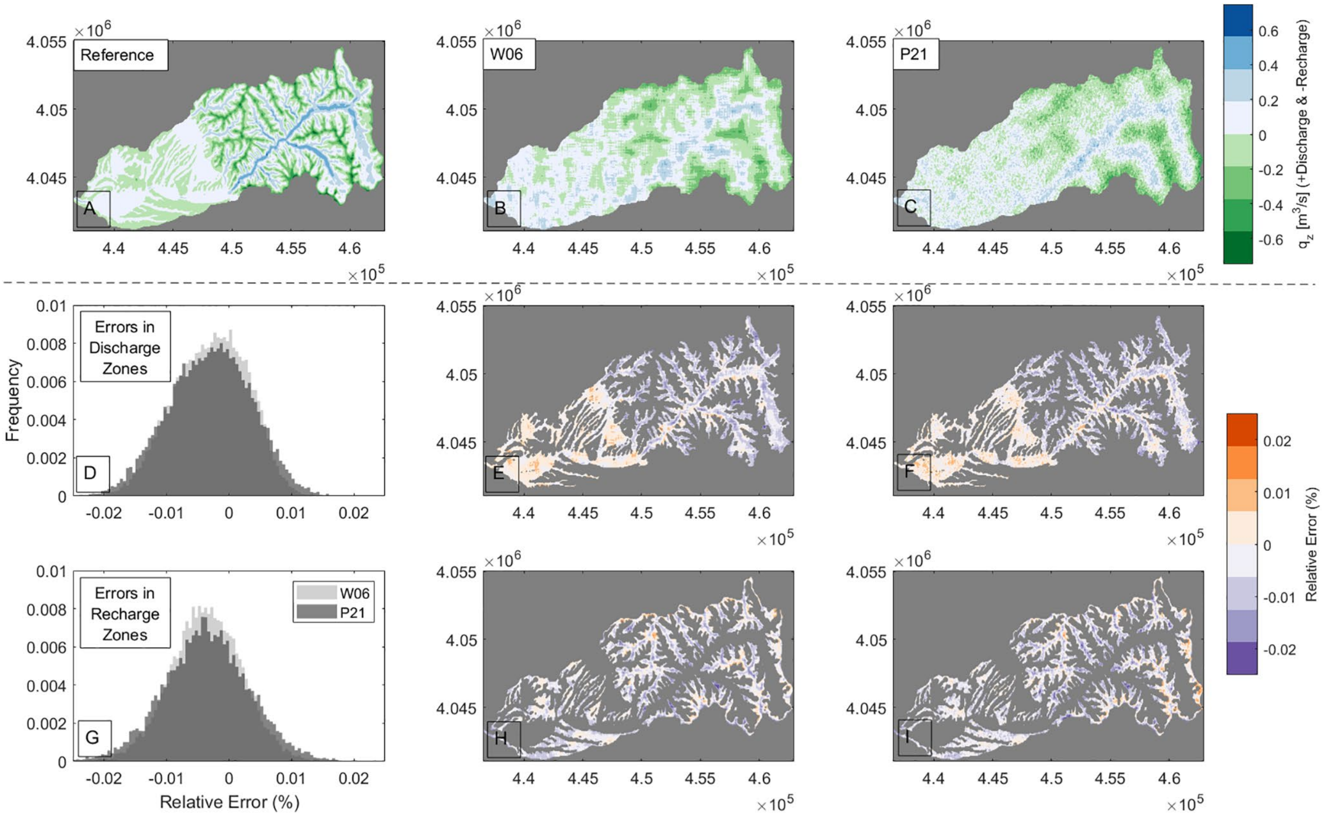

Figure 7. Fluxes in the z-direction on the top layer ($z = 0$) for the Rio Hondo watershed based on the reference model (panel a), W06 (panel b), and P21 (panel c). The relative errors with respect to the reference model for W06 and P21 are shown in the discharge (panels e and f) and recharge (panels h and i) areas. The histogram of relative errors in the discharge and recharge zones are shown in panels d and g, respectively. The relative errors in the discharge or recharge zones are calculated as the ratio of the difference in fluxes between the spectral solution and the reference model over the total discharge or recharge flux estimated over the reference model.

W06 presents a bimodal behavior with a second peak after the 90th percentile, which is not found in either the reference model or P21, which illustrates how the inadequate use of spectral representations of the hydraulic head at the top boundary can lead to erroneous representations of RTDs. A similar situation is observed for the Rio Hondo watershed's RTDs (see panels c and f in Figure 8), where small head gradients controlled by local geomorphic features (e.g., the river network, floodplain configuration, and ridges, among others) are not well captured in the spectral solutions, and therefore, misrepresent the short flow paths and result in an overall control of the longer flow paths.

4.4. Sensitivity to the Number of Spatial Frequencies

We evaluated the effect of the number of Fourier coefficients in W06 and P21 for reconstructing the top boundary hydraulic head and the groundwater fluxes (discharge and recharge) for each case study. To this end, we systematically increased the number of Fourier coefficients until we found minimal improvement in the representation of fluxes relative to the reference model. For the Tothian basin, we evaluate up to 40^2 frequencies, and for the bedforms and Rio Hondo watershed up to 90^2 frequencies. Because the frequencies selected in P21 involve a random sampling of the statistically significant frequencies (Section 2.3 and Equation 5), we performed 10 realizations of P21 for each number of frequencies explored. This provides a quantitative assessment of the effect of the random sampling in Equation 5.

For the Tothian basin, the lowest error in the reconstruction of the top boundary hydraulic head is reached at 16^2 spatial frequencies for P21 and 32^2 spatial frequencies for W06, with no significant improvements when the number of frequencies is increased (Figure 9a). The effect of the random sampling in P21 is negligible after 16^2 frequencies (shaded red bands in Figure 9a). The lowest errors for discharge and recharge fluxes are obtained around 16^2 frequencies with P21 consistently outperforming W06 (Figures 9d and 9e). Similar behavior was found for

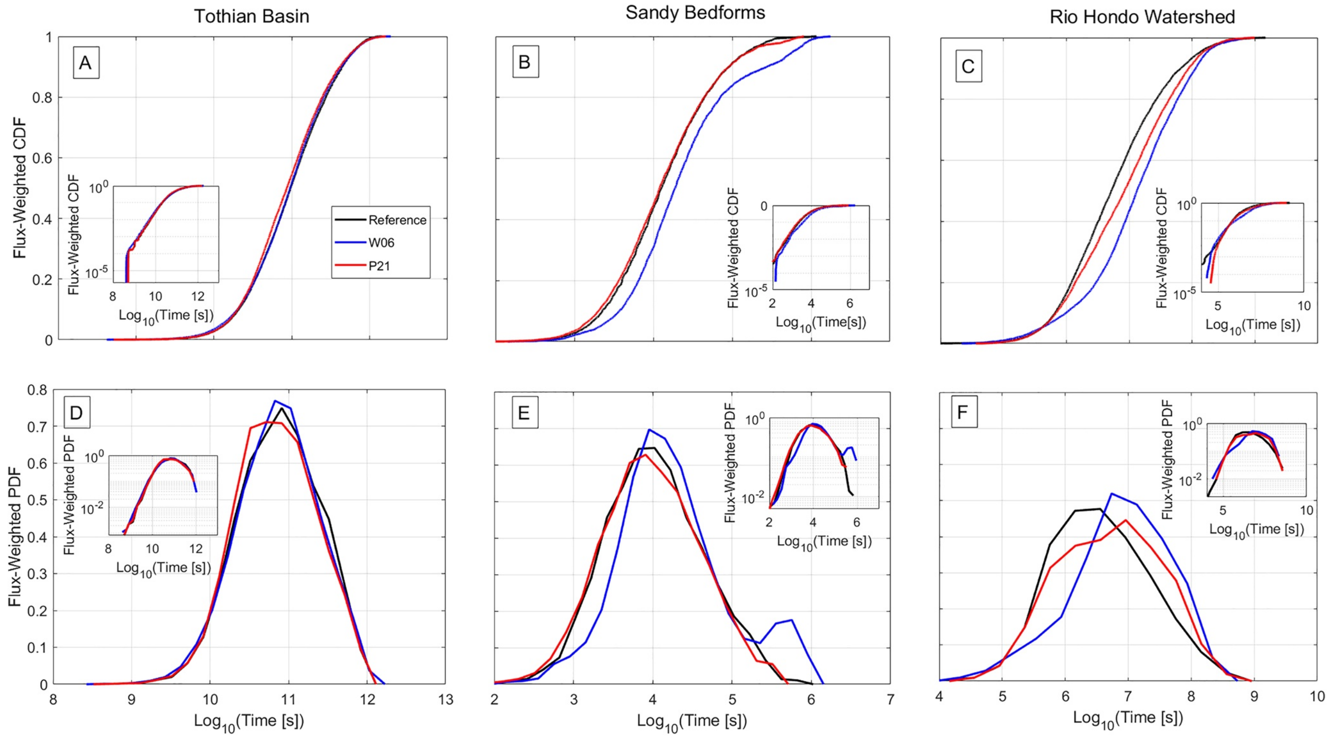

Figure 8. Residence times obtained from the reference model, W06, and P21. Panels a, b, and c show the cumulative distribution functions (CDFs) for the Tothian Basin, Sandy Bedforms, and Rio Hondo Watershed, respectively. Same results in probability density functions (PDFs) are shown in panels d, e, and f. Each panel contains an embedded panel showing the results in logarithmic scale.

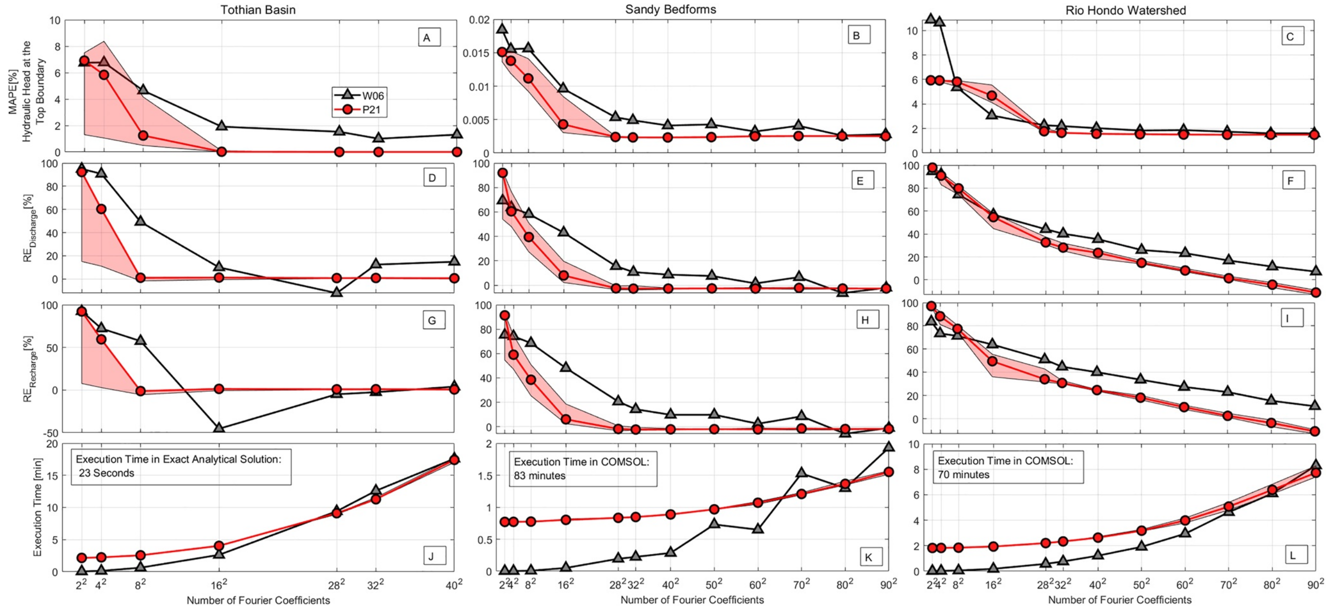

Figure 9. Sensitivity to the number of spatial frequencies used in the spectral solutions for the Tothian Basin, Sandy Bedforms, and Rio Hondo watershed for the W06 (black lines) and P21 (red lines) methods. Panels a–i summarize the errors in the reconstruction of the top boundary hydraulic head (a–c), discharge (d–f), and recharge (g–i). Also, execution times for both approaches are shown in panels j, k, and l. The shaded red bands in each panel represent the envelope of 10 realizations for P21, and the red points correspond to the median value from the realizations. MAPE [%] is the Mean Absolute Percentage Error and RE [%] is the Relative Error estimated as the ratio of the difference between the reference discharge (recharge) and estimated discharge (recharge) over the reference discharge (recharge).

bedforms, where the optimum number of frequencies in P21 is reached at 28^2 frequencies, while for W06 it takes up to 80^2 frequencies to get the same error metrics for the top boundary hydraulic head and groundwater fluxes (Figures 9b–9h). For the Rio Hondo watershed, the top boundary hydraulic head errors stabilize after 28^2 frequencies for both W06 and P21 approaches (MAPE around 2%). Representations with 90^2 spatial frequencies only produce a slight improvement (MAPE around 1.7%, Figure 9c). In contrast, the lowest errors in discharge and recharge fluxes are obtained with 70^2 spatial frequencies for P21 and 90^2 frequencies for W06 (Figures 9f and 9l). This result demonstrates that even slight improvements in the representation of the top hydraulic head can drastically impact the estimation of discharge and recharge fluxes. Increasing frequencies beyond the optimum can result in spurious spatial frequencies that overfit the hydraulic head and radically affect the reconstruction of groundwater fluxes. Typically, this is caused by the disproportionate role of high-frequency features on the hydraulic gradients driving flow. For example, the Rio Hondo watershed is characterized by errors in the recharge and discharge fluxes around $\pm$ 1% for P21 with 70^2 spatial frequencies. When the number of spatial frequencies increases to 90^2, the errors in fluxes increase up to -10%.

Regarding the effect of defining a significance level in P21, we found that the groundwater fluxes in the Tothian basin and bedforms are properly captured with significance levels from 50% to 95%, with the most inferior performance at 0% significance level (see Figure S8 in Supporting Information S1). In contrast, for the case of the Rio Hondo, where dominant frequencies are more randomly distributed in the 2D power spectrum, a random sampling of spatial frequencies (0% significance level) provides a better representation of the groundwater fluxes (see the right column in Figure S8 in Supporting Information S1). This result demonstrates that incorporating dominant frequencies in spectral solutions can significantly improve the estimation of groundwater fluxes, especially for surfaces with well-defined characteristics spatial scales (e.g., periodic basins and bedforms). Conversely, for complex landscapes, such as the Rio Hondo watershed, where multiple important spatial scales are needed to reconstruct the hydraulic head at the top boundary, a random sampling of spatial frequencies in P21 will better describe the total groundwater fluxes.

To assess the computational efficiency of the new spectral solution, we recorded the *execution time* of the functions to run W06 and P21 and the numerical solution using COMSOL in the same workstation. The execution time for W06 is calculated by the sum of the execution time using the codes "Spectop" and "Specvel" reported by Wörman et al. (2006). The execution time for P21 is the sum of the execution time of the function "SS_DomFreq", "SS_Top", and "SS_Vel," (see GitHub repository referenced in Acknowledgments, Samples, and Data Section). The codes are run using a workstation with an 8-Core Intel Xeon and 96 GB of RAM.

The execution times for W06 and P21 increase with the number of frequencies with slightly higher execution times in P21 than W06 (Figures 9j, 9k, and 9l). The difference in execution times between W06 and P21 is caused using the function "SS_DomFreq" in P21, which is required to identify dominant frequencies. Note that the code "SS_DomFreq" generates the spectral power corresponding to a confidence level α derived from Equation 5; therefore, the execution times for exploring different numbers of Fourier coefficients in P21 can be reduced by just executing "SS_DomFreq" once.

Execution times for the Tothian basin using W06 and P21 are around 10 min for 28^2 frequencies and can reach up to 18 min for 40^2 frequencies. In contrast, the execution time for the reference model, based on the exact analytical solution, is 23 s. This benefits from having a closed-form expression, which is the exception rather than the rule (Equation 11). For the sandy bedforms and the Rio Hondo watershed, where COMSOL is used to obtain the numerical solution used as reference, the execution times in W06 and P21 are noticeably lower. For the bedforms, the execution times are less than 2 min for either W06 or P21, while the COMSOL solution takes 83 min. Similar results are found in the Rio Hondo watershed, where the execution times are less than five minutes for the spectral solutions with 70^2 spatial frequencies in contrast to 70 min in COMSOL.

5. Discussion

The reconstruction of the top boundary hydraulic head in periodic (or quasi-periodic) surfaces demonstrates the advantage of using the P21 approach compared with the W06. The use of the auFS spectrum identifies statistically significant spatial frequencies and generally excludes spurious frequencies. Contrariwise, the sbsFS spectrum used in the W06 approach does not guarantee the use of dominant frequencies, and it is likely to increase the spectral leakage. Even though this could be partially addressed by increasing the number of sampled spatial frequencies (increasing the mesh resolution of the sbsFS), the increasing of sampled spatial frequencies with the W06 approach will result in a higher condition number (a matrix closer to singularity) and significant increase in computational burden, which at the same time is likely to add more spurious frequencies to the spatial frequency spectrum. Spurious spatial frequencies improve the goodness of fit at the expense of physical accuracy, creating unrealistic flow cells in the spectral solution. Alternative approaches can be used to improve the reconstruction of the top boundary hydraulic head for specific subregions within the domain of interest. For instance, a mirroring procedure such as the one used by Wörman et al. (2006) can be used to increase the area of analysis to the point where the signal periodicity is a more reasonable assumption (i.e., reduce the boundary effects of a finite domain). Wörman et al. (2006) used this technique to extent their domain of analysis by 16 times. Nevertheless, the use of this mirroring procedure should be used with caution to avoid excessively large matrices for the estimation of Fourier coefficients, which can easily defeat the purpose of this parsimonious and interpretable solution technique. We compared the P21 and W06 approaches for different numbers of Fourier coefficients, demonstrating that the P21 approach requires significantly fewer spatial frequencies than the W06 approach to obtain a proper representation of the top boundary hydraulic head.

Mountainous watersheds, such as the Rio Hondo, do not necessarily exhibit periodic structures and pose a major challenge for the use of spectral solutions. A potential workaround is to increase the number of Fourier coefficients on the spectral analysis; however, as mentioned before, this comes at the expense of computational burden, numerical instability, and spurious spatial frequencies. Also, it is important to note that the spectral decomposition is a continuous approximation of a discrete topographic data set, the DEM, and therefore, it cannot assure a perfect representation of the real topography (Marklund & Wörman, 2011). With this in mind, the spectral solutions for such large natural domains must be understood as an approximation of the average dynamics of groundwater flow and not an exact representation of all the local flow cells, which are driven by steep, local changes of the water table. This opens the door to new strategies that improve spectral solutions over regional domains.

We quantified the benefits of having a better representation of the top boundary hydraulic head on the spectral solution. This improvement is reflected in a better approximation of the hydraulic head and flow fields, as well as the spatial characterization of recharge/discharge areas. We observe that small errors in the reconstruction of the top boundary hydraulic head are amplified in groundwater fluxes derived from the spectral solutions.

The results presented in this study demonstrate that the spectral solutions can represent the RTD of periodic (or quasi-periodic) surfaces such as those exhibited by bedforms. In fact, the spectral solutions can accurately capture the exchange driven by bedform features (e.g., crest planform, transverse and longitudinal wavelength, bedform height, etc.) and their effects on RTDs. These effects can be evaluated from 3-D CFD models (Chen et al., 2018); however, the use of spectral solutions in quasi-periodic structures opens up possibilities by using an interpretable, numerically parsimonious, and reliable approach to explore the nature of the hyporheic exchange process and the role of bed morphology. Regarding regional scales, such as the Rio Hondo watershed, the spectral solutions, and their resulting fluxes and RTD can be used to gain insight but should be used and interpreted with caution. The Rio Hondo watershed illustrates the limitations of spectral decomposition approaches to capture all the relevant spatial scales characterizing complex landscapes. That said, the P21 approach partially addresses some of these limitations, and it still represents an advance toward a reasonable approximation of a complex flow field.

6. Conclusions

This study contributes to the improvement of the previously proposed and widely used framework for the use of spectral solutions of the groundwater flow equation (Wörman et al., 2006). We proposed a rigorous approach to select frequencies in the pre-assigned spatial frequency spectrum. The solutions are aimed to be implemented when a reasonable approximation of the hydraulic head at the top boundary is available or can be assumed. For example, the case of topography-controlled regional groundwater flow (Haitjema & Mitchell-Bruker, 2005) and bedform-driven hyporheic exchange in stream sediments (Elliott & Brooks, 1997a, 1997b). The former case is typical of humid regions where the water table can be considered as a subdued and smoothed version of the topography (Gleeson et al., 2011). Three specific findings are summarized as follows

1. A priori inclusion of dominant frequencies in the pre-assigned spatial frequency spectrum significantly improves the representation of the top boundary hydraulic head of quasiperiodic surfaces, such as those in ripples and dunes, and therefore the performance of the spectral solutions of the groundwater flow equation. The

benefit, however, is minor for large-scale landscapes characterized by multiple spatial scales, as illustrated by our results in the Rio Hondo watershed testbed.

2. While improvements in the representation of the top boundary condition by including dominant frequencies seem to be minor (with changes in relative errors less than 1%), significant changes are observed in the magnitude of discharge and recharge fluxes with changes in relative errors up to −12% in the synthetic periodic basin, up to 20% for sandy bedforms, and up to 12% for the Rio Hondo watershed. Although the magnitude of discharge and recharge fluxes in the Rio Hondo watershed are well represented with the new approach (relative errors close to −3%), the spatial patterns of fluxes are misrepresented because of the spectral decomposition's inability to capture sharp increases in high-gradient areas such as the landscape ridges and river network.
3. The RTDs derived in the synthetic periodic basin for both approaches are similar, even though they present significant differences in fluxes at the top boundary, and accurately reproduce the reference solution. We argue that for this simple system both approaches capture the overall regional patterns of flow, which dominate this system's RTD. For more complex scenarios, such as bedforms, the RTDs are drastically improved by the inclusion of dominant frequencies, demonstrating the need to capture dominant spatial scales for the spectral solutions. The RTDs for the Rio Hondo watershed with both spectral approaches are characterized by older residence times than the reference solution, which is likely caused by the spectral methods' inability to resolve local head gradients and their resulting flow cells.

The solutions presented here assume a homogeneous and isotropic porous media; however, solutions for depth-decaying, anisotropic and layered permeability, such as the ones presented by Marklund and Wörman (2011)**,** could be implemented with the our proposed approach. In general, the spectral solutions provide a useful tool for preliminary and quick assessments of the groundwater systems for small and large domains. Their interpretability makes them a useful tool to gain mechanistic understanding about the effects of complex topographic or bathymetric variations in the evolution of exchange fluxes and residence times, which ultimately control both chemical and biochemical processes.

Data Availability Statement

The scripts implemented for the analysis of spectral solutions with dominant frequencies are publicly available at https://doi.org/10.5281/zenodo.5717479. Supporting Information provides a detailed derivation of the spectral solutions and additional results for the spectral analysis of the sandy bedforms and the Rio Hondo watershed.

Acknowledgments
This study was supported by the U.S. Department of Energy, Office of Science, Office of Biological and Environmental Research, Environmental System Science (ESS) program through subcontract to the River Corridor Scientific Focus Area project at Pacific Northwest National Laboratory. Additional support was provided by the U.S. National Science Foundation (awards EAR-1830172 and OIA-2020814).

References

Bear, J. (1975). Dynamics of fluids in porous media. *Soil Science*, *120*(2), 162–163. https://doi.org/10.1097/00010694-197508000-00022
Boano, F., Demaria, A., Revelli, R., & Ridolfi, L. (2010). Biogeochemical zonation due to intrameander hyporheic flow. *Water Resources Research*, *46*(2), 1–13. https://doi.org/10.1029/2008WR007583
Boano, F., Harvey, J. W., Marion, A., Packman, A. I., Revelli, R., Ridolfi, L., & Wörman, A. (2014). Hyporheic flow and transport processes: Mechanisms, models, and biogeochemical implications. *Reviews of Geophysics*, *52*(4), 603–679. https://doi.org/10.1002/2012RG000417
Cardenas, M. B. (2008). Surface water-groundwater interface geomorphology leads to scaling of residence times. *Geophysical Research Letters*, *35*(8), L08402. https://doi.org/10.1029/2008GL033753
Caruso, A., Ridolfi, L., & Boano, F. (2016). Impact of watershed topography on hyporheic exchange. *Advances in Water Resources*, *94*, 400–411. https://doi.org/10.1016/j.advwatres.2016.06.005
Chen, X., Cardenas, M. B., & Chen, L. (2018). Hyporheic exchange driven by three-dimensional sandy bed forms: Sensitivity to and prediction from bed form geometry. *Water Resources Research*, *54*(6), 4131–4149. https://doi.org/10.1029/2018WR022663
Chow, R., Wu, H., Bennett, J. P., Dugge, J., Wöhling, T., & Nowak, W. (2019). Sensitivity of simulated hyporheic exchange to River Bathymetry: The Steinlach River Test Site. *Groundwater*, *57*(3), 378–391. https://doi.org/10.1111/gwat.12816
Condon, L. E., & Maxwell, R. M. (2015). Evaluating the relationship between topography and groundwater using outputs from a continental-scale integrated hydrology model. *Water Resources Research*, *51*(8), 6602–6621. https://doi.org/10.1002/2014WR016774
Crockett, R. (2019). *A primer on Fourier analysis for the geosciences*. Cambridge University Press. https://doi.org/10.1017/9781316543818
Elliott, A. H., & Brooks, N. H. (1997a). Transfer of nonsorbing solutes to a streambed with bed forms: Laboratory experiments. *Water Resources Research*, *33*(1), 137–151. https://doi.org/10.1029/96WR02783
Elliott, A. H., & Brooks, N. H. (1997b). Transfer of nonsorbing solutes to a streambed with bed forms: Theory. *Water Resources Research*, *33*(1), 123–136. https://doi.org/10.1029/96WR02784
Fehlman, H. M. (1985). *Resistance components and velocity distributions of open channel flows over bedforms*.
Fournier, A., Fussell, D., & Carpenter, L. (1982). Graphics and image processing computer rendering of Stochastic models. *Communications of the ACM*, *25*(6), 371–384. https://doi.org/10.1145/358523.358553

Frisbee, M. D., Phillips, F. M., Campbell, A. R., Liu, F., & Sanchez, S. A. (2011). Streamflow generation in a large, alpine watershed in the southern Rocky Mountains of Colorado: Is streamflow generation simply the aggregation of hillslope runoff responses? *Water Resources Research*, *47*(6), 1–18. https://doi.org/10.1029/2010WR009391

Frisbee, M. D., Wilson, J. L., Gomez-Velez, J. D., Phillips, F. M., & Campbell, A. R. (2013). Are we missing the tail (and the tale) of residence time distributions in watersheds? *Geophysical Research Letters*, *40*(17), 4633–4637. https://doi.org/10.1002/grl.50895

Gleeson, T., Marklund, L., Smith, L., & Manning, A. H. (2011). Classifying the water table at regional to continental scales. *Geophysical Research Letters*, *38*(5). https://doi.org/10.1029/2010gl046427

Gomez-Velez, J. D., & Harvey, J. W. (2014). A hydrogeomorphic river network model predicts where and why hyporheic exchange is important in large basins. *Geophysical Research Letters*, *41*(18), 6403–6412. https://doi.org/10.1002/2014GL061099

Gomez-Velez, J. D., Wilson, J. L., Cardenas, M. B., & Harvey, J. W. (2017). Flow and residence times of dynamic river bank storage and sinuosity-driven hyporheic exchange. *Water Resources Research*, *53*(10), 8572–8595. https://doi.org/10.1002/2017WR021362

Gomez, J. D., & Wilson, J. L. (2013). Age distributions and dynamically changing hydrologic systems: Exploring topography-driven flow. *Water Resources Research*, *49*(3), 1503–1522. https://doi.org/10.1002/wrcr.20127

Gomez, J. D., Wilson, J. L., & Cardenas, M. B. (2012). Residence time distributions in sinuosity-driven hyporheic zones and their biogeochemical effects. *Water Resources Research*, *48*(9), 2012WR012180. https://doi.org/10.1029/2012WR012180

Haitjema, H. M., & Mitchell-Bruker, S. (2005). Are water tables a subdued replica of the topography? *Ground Water*, *43*(6), 050824075421008. https://doi.org/10.1111/j.1745-6584.2005.00090.x

Hallet, B. (1990). Spatial self-organization in geomorphology: From periodic bedforms and patterned ground to scale-invariant topography. *Earth-Science Reviews*, *29*(1–4), 57–75. https://doi.org/10.1016/0012-8252(0)90028-T

Harvey, J. W. (2016). Hydrologic exchange flows and their ecological consequences in river corridors. In J. B. Jones & E. Stanley (Eds.), *Stream ecosystems in a changing environment* (pp. 1–83). Elsevier. https://doi.org/10.1016/B978-0-12-405890-3.00001-4

Harvey, J., Gomez-Velez, J., Schmadel, N., Scott, D., Boyer, E., Alexander, R., et al. (2019). How hydrologic connectivity regulates water quality in river corridors. *JAWRA Journal of the American Water Resources Association*, *55*(2), 369–381. https://doi.org/10.1111/1752-1688.12691

Harvey, J., & Gooseff, M. (2015). River corridor science: Hydrologic exchange and ecological consequences from bedforms to basins. *Water Resources Research*, *51*(9), 6893–6922. https://doi.org/10.1002/2015WR017617

Heath, R. C. (1983). *Basic ground-water hydrology*. US Geological Survey Water Supply Paper. https://doi.org/10.3133/wsp2220

Hoerl, A. E., & Kennard, R. W. (1970). Ridge regression: Applications to nonorthogonal problems. *Technometrics*, *12*(1), 69–82. https://doi.org/10.1080/00401706.1970.10488635

Ho, C. H., & Lin, C. J. (2012). Large-scale linear support vector regression. *Journal of Machine Learning Research*, *13*, 3323–3348. https://doi.org/10.5555/2503308.2503348

Knapp, K. C., Weinberg, M., Howitt, R., & Posnikoff, J. F. (2003). Water transfers, agriculture, and groundwater management: A dynamic economic analysis. *Journal of Environmental Management*, *67*(4), 291–301. https://doi.org/10.1016/S0301-4797(02)00162-7

Kreyszig, E. (2014). Advanced engineering mathematics. In *Higher engineering mathematics*. BS Grewal.

Kuo, W.-L., Steenhuis, T. S., McCulloch, C. E., Mohler, C. L., Weinstein, D. A., DeGloria, S. D., & Swaney, D. P. (1999). Effect of grid size on runoff and soil moisture for a variable-source-area hydrology model. *Water Resources Research*, *35*(11), 3419–3428. https://doi.org/10.1029/1999WR900183

Kutz, J. N. (2013). In O. U. Press (Ed.), *Data-driven modeling & scientific computation: Methods for complex systems & big data* (1st ed.). Oxford University Press.

Maher, K., & Chamberlain, C. P. (2014). Hydrologic regulation of chemical weathering and the geologic carbon cycle. *Science*, *343*(6178), 1502–1504. https://doi.org/10.1126/science.1250770

Mallat, S. (2008). *A wavelet tour of signal processing: The sparse way*. (3rd ed.). Academic Press.

Marklund, L., & Wörman, A. (2011). The use of spectral analysis-based exact solutions to characterize topography-controlled groundwater flow. *Hydrogeology Journal*, *19*(8), 1531–1543. https://doi.org/10.1007/s10040-011-0768-4

Mojarrad, B. B., Riml, J., Wörman, A., & Laudon, H. (2019). Fragmentation of the hyporheic zone due to regional groundwater circulation. *Water Resources Research*, *55*, 1242–1262. https://doi.org/10.1029/2018WR024609

Packman, A. I., & Bencala, K. E. (2000). Modeling surface–subsurface hydrological interactions. In *Streams and ground waters* (pp. 45–80). Elsevier. https://doi.org/10.1016/B978-012389845-6/50003-X

Percival, D. B., & Walden, A. T. (1993). *Spectral analysis for physical applications*. Cambridge University Press.

Perron, J. T., Kirchner, J. W., & Dietrich, W. E. (2008). Spectral signatures of characteristic spatial scales and nonfractal structure in landscapes. *Journal of Geophysical Research: Earth Surface*, *113*(4), 1–14. https://doi.org/10.1029/2007JF000866

Rubin, D. M., & Carter, C. L. (2005). *MATLAB code for simulating bedforms and cross-bedding*.

Shen, H. W., Fehlman, H. M., & Mendoza, C. (1990). Bed form resistances in open channel flows. *Journal of Hydraulic Engineering*, *116*(6), 799–815. https://doi.org/10.1061/(asce)0733-9429(1990)116:6(799)

Shen, C., Riley, W. J., Smithgall, K. R., Melack, J. M., & Fang, K. (2016). The fan of influence of streams and channel feedbacks to simulated land surface water and carbon dynamics. *Water Resources Research*, *52*(2), 880–902. https://doi.org/10.1002/2015WR018086

Singh, T., Gomez-velez, J. D., Wu, L., Wörman, A., Hannah, D. M., & Krause, S. (2020). Effects of successive peak - flow events on hyporheic exchange and residence times Effects of successive peak-flow events on hyporheic exchange and residence times. *Water Resources Research*, *56*(8). https://doi.org/10.1029/2020WR027113

Singh, T., Wu, L., Gomez-Velez, J. D., Lewandowski, J., Hannah, D. M., & Krause, S. (2019). Dynamic hyporheic zones: Exploring the role of peak flow events on bedform-induced hyporheic exchange. *Water Resources Research*, *55*(1), 218–235. https://doi.org/10.1029/2018WR022993

Stoertz, M. W., & Bradbury, K. R. (1989). Mapping recharge areas using a ground-water flow model – A case study. *Ground Water*, *27*(2), 220–228. https://doi.org/10.1111/j.1745-6584.1989.tb00443.x

Stonedahl, S. H., Harvey, J. W., AndersSalehin, M., Packman, A. I., & Packman, A. I. (2010). A multiscale model for integrating hyporheic exchange from ripples to meanders. *Water Resources Research*, *46*(12), 1–14. https://doi.org/10.1029/2009WR008865

Stonedahl, S. H., Harvey, J. W., & Packman, A. I. (2013). Interactions between hyporheic flow produced by stream meanders, bars, and dunes. *Water Resources Research*, *49*(9), 5450–5461. https://doi.org/10.1002/wrcr.20400

Sulis, M., Paniconi, C., & Camporese, M. (2011). Impact of grid resolution on the integrated and distributed response of a coupled surface-subsurface hydrological model for the des Anglais catchment, Quebec. *Hydrological Processes*, *25*(12), 1853–1865. https://doi.org/10.1002/hyp.7941

Toth, J. (1962). A theory of groundwater motion in small drainage basins in central Alberta, Canada. *Journal of Geophysical Research*, *67*(11), 4375–4388. https://doi.org/10.1029/jz067i011p04375

Toth, J. (1963). A theoretical analysis of groundwater flow in small drainage basins 1 of phe - low order stream and having similar t he outlet of lowest impounded body of a relatively. *Journal of Geophysical Research*, *68*(16), 4795–4812. https://doi.org/10.1029/JZ068i016p04795

Tóth, J. (2009). In F. A. O. of the UN (Ed.), *Gravitational systems of groundwater flow: Theory, evaluation, utilization*. Cambridge University Press.

Wang, C., Gomez-Velez, J. D., & Wilson, J. L. (2018). The importance of capturing topographic features for modeling groundwater flow and transport in mountainous watersheds. *Water Resources Research*, *54*(12), 10313–10338. https://doi.org/10.1029/2018WR023863

Wang, C., Gomez-Velez, J. D., & Wilson, J. L. (2021). Dynamic coevolution of baseflow and multiscale groundwater flow system during prolonged droughts. *Journal of Hydrology*.

Wang, J. Z., Wörman, A., Bresciani, E., Wan, L., Wang, X. S., & Jiang, X. W. (2016). On the use of late-time peaks of residence time distributions for the characterization of hierarchically nested groundwater flow systems. *Journal of Hydrology*, *543*, 47–58. https://doi.org/10.1016/j.jhydrol.2016.04.034

White, A. F., & Brantley, S. L. (2003). The effect of time on the weathering of silicate minerals: Why do weathering rates differ in the laboratory and field? *Chemical Geology*, *202*(3–4), 479–506. https://doi.org/10.1016/j.chemgeo.2003.03.001

Winter, T. C., Harvey, J. W., Franke, O. L., & Alley, W. M. (1998). Ground water and surface water: A single resource. *Circular*. https://doi.org/10.3133/cir1139

Wolock, D. M., & Price, C. V. (1994). Effects of digital elevation model map scale and data resolution on a topography-based watershed model. *Water Resources Research*, *30*(11), 3041–3052. https://doi.org/10.1029/94WR01971

Wörman, A., Packman, A. I., Marklund, L., Harvey, J. W., & Stone, S. H. (2006). Exact three-dimensional spectral solution to surface-groundwater interactions with arbitrary surface topography. *Geophysical Research Letters*, *33*(7), 2–5. https://doi.org/10.1029/2006GL025747

Wörman, A., Packman, A. I., Marklund, L., Harvey, J. W., & Stone, S. H. (2007). Fractal topography and subsurface water flows from fluvial bedforms to the continental shield. *Geophysical Research Letters*, *34*(7), 1–5. https://doi.org/10.1029/2007GL029426

Wu, L., Gomez-Velez, J. D., Krause, S., Singh, T., Wörman, A., & Lewandowski, J. (2020). Impact of flow alteration and temperature variability on hyporheic exchange. *Water Resources Research*, *56*(3). https://doi.org/10.1029/2019WR026225

Wu, L., Singh, T., Gomez-Velez, J., Nützmann, G., Wörman, A., Krause, S., & Lewandowski, J. (2018). Impact of dynamically changing discharge on hyporheic exchange processes under gaining and losing groundwater conditions. *Water Resources Research*, *54*(12), 10076–10093. https://doi.org/10.1029/2018WR023185

Zarnetske, J. P., Haggerty, R., Wondzell, S. M., & Baker, M. A. (2011). Dynamics of nitrate production and removal as a function of residence time in the hyporheic zone. *Journal of Geophysical Research*, *116*(G1), G01025. https://doi.org/10.1029/2010JG001356

Zarnetske, J. P., Haggerty, R., Wondzell, S. M., Bokil, V. A., & González-Pinzón, R. (2012). Coupled transport and reaction kinetics control the nitrate source-sink function of hyporheic zones. *Water Resources Research*, *48*(11), 1–15. https://doi.org/10.1029/2012WR011894

Zijl, W. (1999). Scale aspects of groundwater flow and transport systems. *Hydrogeology Journal*, *7*(1), 139–150. https://doi.org/10.1007/s100400050185